國立臺灣大學工學院材料科學與工程學系

碩士論文

Department of Material Science and Engineering

College of Engineering

National Taiwan University

Master’s Thesis

傾斜磁異向性在鉑/鈷/鉑異直結構中對自旋軌道矩無場翻轉的影響

The Effect of Tilted Magnetic Anisotropy on Field-Free Spin-Orbit Torque Switching in Pt/Co/Pt Heterostructures

林孟頡

Meng-Chieh Lin

指導教授：白奇峰 博士

Advisor: Chi-Feng Pai, Ph.D.

中華民國 113 年 7 月

July, 2024

doi:10.6342/NTU202403259

國立臺灣大學碩士學位論文
口試委員會審定書
MASTER'S THESIS ACCEPTANCE CERTIFICATE
NATIONAL TAIWAN UNIVERSITY

（論文中文題目） (Chinese title of Master's Thesis)	傾斜磁異向性在鉑/鈷/鉑異質結構中對自旋軌道矩無場翻轉的影響
（論文英文題目） (English title of Master's Thesis)	The Effect of Tilted Magnetic Anisotropy on Field-Free Spin-Orbit Torque Switching in Pt/Co/Pt Heterostructures

本論文係 **林孟頡** (R11527078) 在國立臺灣大學材料科學與工程學系、所完成之碩士學位論文，於民國 113 年 7 月 29 日承下列考試委員審查通過及口試及格，特此證明。

The undersigned, appointed by the Department / Graduate Institute of Materials Science and Engineering on 29th/July/2024 have examined a Master's Thesis entitled above presented by **Lin, Meng-Chieh** (R11527078) candidate and hereby certify that it is worthy of acceptance.

口試委員
Oral examination committee:

白奇峰 白奇峰
（指導教授 Advisor）

魏拯華 魏拯華

薛文証 薛文証

系（所、學位學程）主管 Director： 蔡豐羽 蔡豐羽

誌謝

首先感謝台大工學院，提供了一個很棒的機會在這邊就讀材料所碩士班，讓我在碩士生涯中擴展我的專業知識，包括金屬材料，生醫材料，高分子材料與半導體材料等多方面的領域。感謝白奇峰老師收我當學生，讓我能在 SCREAM TEAM 裡面學習並研究自旋電子與磁性材料，進而培養閱讀文獻、實驗設計、材料製程、磁性量測、數據分析及報告撰寫的能力，使我收穫良多。也感謝奈米機電中心與相關人員，教導我如何操作分段式旋塗機以及 MA8 曝光機以及實驗時的注意事項，並提供乾淨優良的實驗環境。

首先要感謝黃宇豪學長，在我進實驗室教我各個器材如 sputter、GMW 的操作方法與實驗技巧，以及磁性材料的許多原理與知識，讓我能夠快速步上軌道並獨立的完成實驗，也在我後續實驗有疑問時能夠提供看法與思路，協助我解決問題，還有在 Origin 的操作上，也告訴我許多技巧，讓我能妥善的處理數據。也感謝廖唯邦、胡宸瑜學長、劉彥廷學長、林俊逸學長等博士生，在我操作儀器遇到問題時都能悉心教導並提供協助。

另外也要感謝同屆的博士生韓瑞旭和吉冠宇，教我許多理論方面的知識，還有一些儀器的操作與實驗方法。感謝同屆的林聖文同學、徐沛汝同學和黃文翰同學，能夠陪伴我的碩士班生活並提供我精神上的支柱，建立深厚的友誼。感謝黎哲睿學弟、黃書鋒學弟、鍾詠絢學妹和洪翊文學弟，能夠一起進行課外活動並活絡實驗室的氣氛。

最後感謝我的家人，我的父母一路支持我求學的路途，永遠作為我的避風港，做我最堅實的靠山。感謝我的女友給我心靈上的支持與依靠，還有我前進的動力。希望我畢業以後能夠不忘本心，利用所學貢獻社會，努力朝夢想邁進。

摘要

隨著物聯網(IOT)設備與高性能計算(HPC)的需求增加，使得磁性記憶體逐漸受到重視。由於電流注入的幾何結構差異，相較於現今量產主流的自旋轉移矩記憶體(STT-MRAM)，自旋軌道矩記憶體(SOT-MRAM)擁有更高的開關速度以及耐用性，但是要實際應用於元件中，我們需要提供外加磁場來打破對稱性以實現磁性的確定性的磁性切換。目前有一種無場翻轉方案是透過在濺鍍過程中將重金屬層斜向生長，以傾斜垂直磁異向性(tilted PMA)。我進一步測試了在鉭/鉑/鈷/鉑/鉭(Ta/Pt/Co/Pt/Ta)不同層之間的斜向生長對於無場翻轉的影響，並且發現了組合不同的斜向生長層可以進一步提高無場翻轉比率並降低翻轉的電流。再經由不同角度的磁滯曲線偏移，可以驗證是由傾斜磁垂直異向性導致的。隨後也探討了退火對於斜向生長鉑晶格結構與無場翻轉的影響，發現退火帶來的原子重新排列與混合會破壞傾斜磁異向性的形成，如何在退火後保留傾斜磁異向性甚至透過退火增強會是一個具有發展潛力的課題。

關鍵字：自旋軌道矩、自旋霍爾效應、無場翻轉、傾斜磁異向性、磁性材料、磁性記憶體

doi:10.6342/NTU202403259

Abstract

With the increasing demand for Internet of Things (IoT) devices and high-performance computing (HPC), magnetic memory is gaining attention. Due to the differences in the geometry of current injection, Spin Orbit Torque Magnetic Random Access Memory (SOT-MRAM) offers higher switching speeds and durability compared to the mainstream Spin Transfer Torque MRAM (STT-MRAM) currently in mass production. However, for practical application in devices, an external magnetic field is required to break symmetry for deterministic magnetic switching. Currently, a field-free switching scheme involves the oblique growth of the heavy metal layer during sputtering to tilt the perpendicular magnetic anisotropy (tilted PMA). I further tested the effects of oblique growth between different layers of tantalum /platinum /cobalt /platinum /tantalum on field-free switching and found that combining different obliquely grown layers can further improve the field-free switching ratio and reduce the switching current. Shifts in the hysteresis curves at different angles verify that this is caused by the tilted perpendicular magnetic anisotropy. Subsequently, the effects of annealing on the lattice structure of obliquely grown Pt and field-free switching were also investigated. It was found that the atomic rearrangement and mixing caused by annealing disrupt the formation of tilted magnetic anisotropy. How to retain the tilted magnetic anisotropy after annealing, or even enhance it through annealing, will be a promising topic for further development.

Keywords: Spin Orbit Torque, Spin Hall Effect, Field-Free Switching, Tilted Magnetic

doi:10.6342/NTU202403259

Anisotropy, Magnetic Materials, Magnetic Memory

.

Contents

doi:10.6342/NTU202403259

doi:10.6342/NTU202403259

List of figures

doi:10.6342/NTU202403259

List of tables

doi:10.6342/NTU202403259

Chapter 1 Introduction

1.1 Magnetoresistive Random Access Memory

Magnetoresistive Random Access Memory (MRAM) is a type of non-volatile memory technology that uses magnetic states to store data. Unlike traditional memory technologies (DRAM and SRAM) which require power to maintain the stored information, MRAM retains data even when the power is off, making it a persistent memory. This provides a significant advantage in applications where data persistence is crucial, such as in embedded systems, automotive electronics, and wearables.

The mechanism of MRAM is that resistance of a material changes in response to a magnetic field. This effect is utilized to detect and manipulate the magnetic orientation of the ferromagnetic layers within the MRAM device.

In MRAM, data is stored in magnetic cells. Each cell consists of a magnetic tunnel junction (MTJ), which is composed of two ferromagnetic layers separated by a thin insulating layer (often made of MgO). One of the ferromagnetic layers is magnetically fixed, or pinned, while the orientation of the other layer (the free layer) can be manipulated to represent data (0s and 1s). The read operation in MRAM is performed by measuring the resistance of the MTJ. If the magnetic layers are parallel, the resistance is low, indicating a '1'. If they are antiparallel, the resistance is high, indicating a '0'. Writing data in MRAM involves changing the magnetic orientation of the free layer. This can be achieved using magnetic fields, spin-polarized current (Spin Transfer Torque, STT), or Spin Orbit Torque (SOT).

doi:10.6342/NTU202403259

Types of MRAM

Field-Induced MRAM: The earliest form of MRAM, which uses external magnetic fields to write data. This method is less common today due to scalability and power efficiency challenges.

Spin Transfer Torque MRAM (STT-MRAM) uses a spin-polarized current to switch the magnetic orientation of the free layer. STT-MRAM offers better scalability and lower power consumption than field-induced one, making it suitable for broader applications.

Spin Orbit Torque MRAM (SOT-MRAM) is the newest technology that uses spin-orbit coupling to switch the magnetic state. SOT-MRAM potentially offers faster switching speeds and lower power consumption than STT-MRAM.

MRAM is considered a promising technology for various applications, including enterprise storage, in memory computing (Fig.1.1b), AI, and any other application requiring quick, persistent storage.

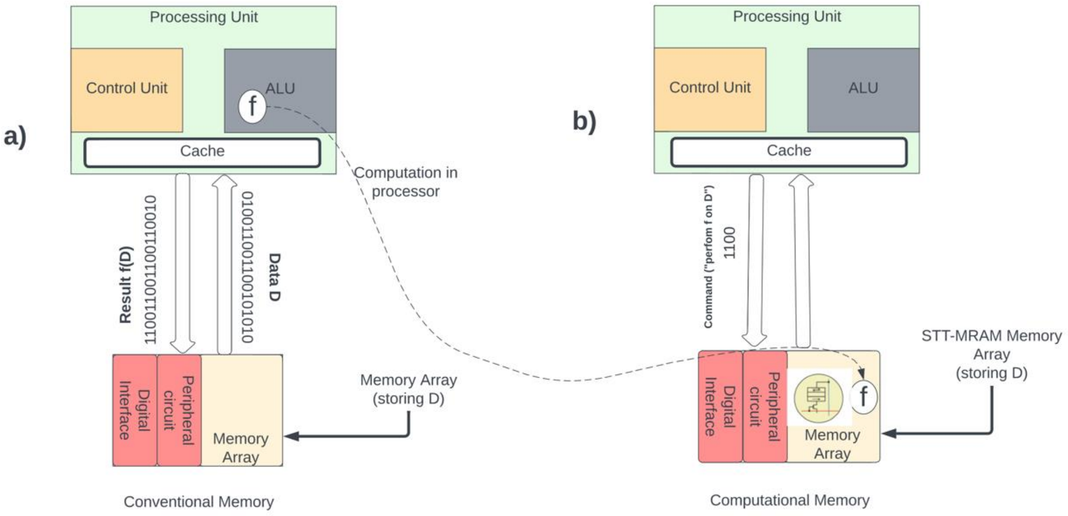

Figure 1. 1: (a) Typical von Neumann architecture and (b) in-memory computing architecture. F indicates function. [9]

1.2 Magnetism

1.2.1 Paramagetism

When certain materials which are weakly attracted by an external magnetic field and form internal induced magnetic fields in the direction of the applied field (Fig.1.2). This effect is unlike ferromagnetism where permanent magnets are created, they do not retain magnetization when external magnetic field is removed because of the thermal motion disarranges the spin orientations.

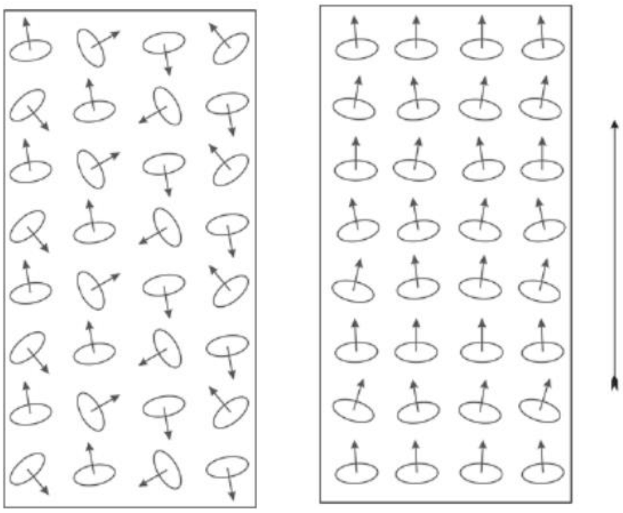

Figure 1. 2: Illustration of paramagnetism. [2]

When the temperature is even higher, the thermal motion makes the atom more disorder. The alignment of the magnetic moment was randomized under phase transformation so that ferromagnetic and ferrimagnetic will turn into paramagnetic. This is called the Curie temperature T_C [3]. The magnetic susceptibility χ above T_C is given by Curie-Weiss Law [5] :

$$\chi = \frac{C}{T - T_C} \ or \ M = C\frac{H}{T - T_C} \qquad (1.1)$$

doi:10.6342/NTU202403259

where C represents the Curie constant.

1.2.2 Diamagnetism

When a magnetic field is applied on certain material, it induces a magnetic field in an opposite direction of the applied field, generates a repulsive force, the phenomenon is called diamagnetism. This can be considered as Lenz's Law: There are two electron orbits, one moving clockwise and the other counterclockwise. When an external magnetic field is applied in the direction entering the page, it increases the centripetal force for the clockwise-moving electron, thereby increasing its magnetic moment directed out of the page, and vice versa. The net effect will be repulsive and the magnetic susceptibility χ will be negative. All materials have diamagnetism even for the ferromagnetic and paramagnetic ones, but it is weak to be overcome by other magnetic effects.

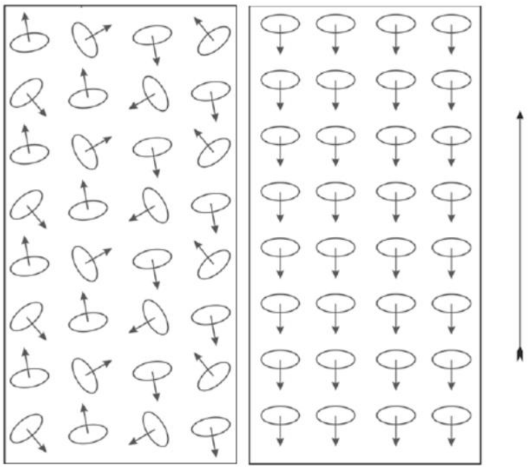

Figure 1. 3: Illustration of diamagnetism [2]

1.2.3 Ferromagnetism

In ferromagnetic materials there are many unpaired electrons. Due to exchange interactions [1], the spins of these electrons tend to align in the same direction as adjacent unpaired electrons. There are many magnetic domains and within each domain all

doi:10.6342/NTU202403259

electron spins are aligned in one direction, creating a "saturated magnetic moment". Since the direction and magnitude of magnetic moments differ between domains, the net magnetic moment and magnetization vector of an unmagnetized ferromagnetic material is almost zero. When an external magnetic field is applied, the magnetic moments of these domains tend to align with the direction of the external field, forming a strong magnetization vector and its induced field (Fig.1.4).

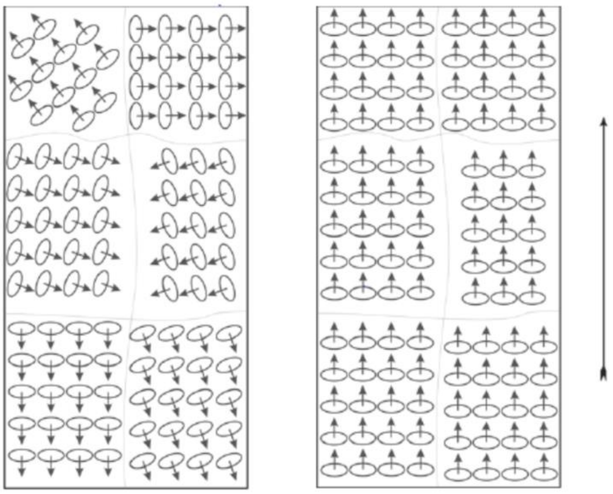

Figure 1. 4: Before and after magnetic field applied on a ferromagnetic material.[2]

As the external field increases, the magnetization intensity also increases, until it reaches the "saturation point" where the net magnetic moment equals the saturated magnetic moment. At this point, further increasing the external magnetic field will not change the magnetization intensity. If the external magnetic field is reduced, the magnetization intensity will also decrease, but it will not match the previous magnetization intensity for the same external magnetic field. The curve of magnetization intensity versus external magnetic field forms a hysteresis loop (Fig .1.5). Consider exchange interaction and must have unfilled electron shells, only Fe, Co and Ni are ferromagnet in room temperature.

doi:10.6342/NTU202403259

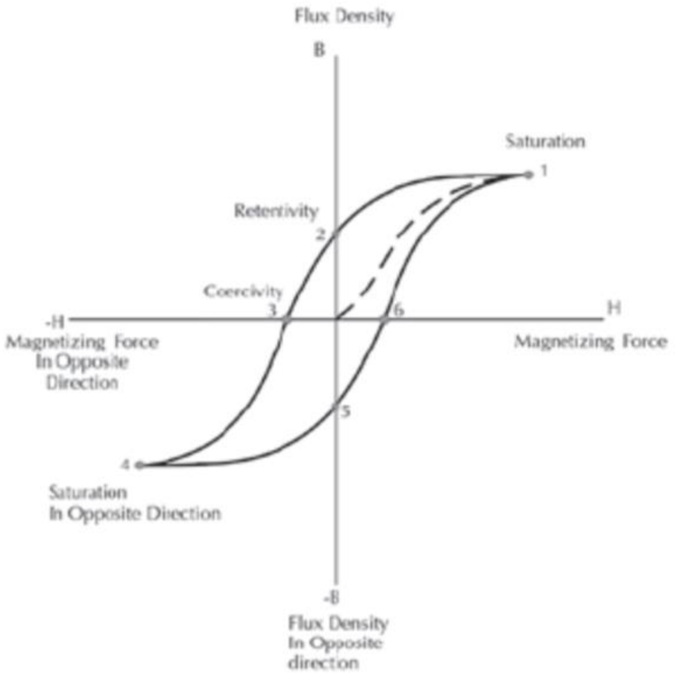

Figure 1. 5: Hysteresis loop of magnetization. [2]

1.2.4 Antiferromagnetism

Louis Néel discovered antiferromagnetic material at the 1930s. Due to exchange coupling, the magnetic moment tends to align. However, unlike ferromagnetic, the moments align in an antiparallel way meaning that the spin orientation of neighboring electron is opposite (Fig.1.6a), making both the total magnetization and magnetic susceptibility χ close to zero. By specific material design, non-colinear antiferromagnet (Fig 1.6b) can be realized with non-parallel moment orientation but zero total magnetization [6].

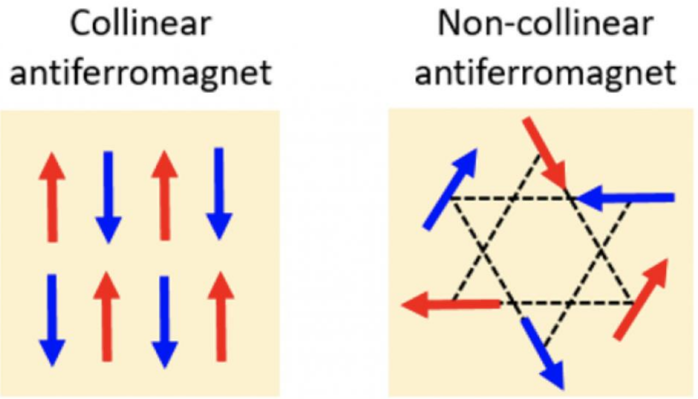

Figure 1. 6: Collinear and non-collinear antiferromagnet [6]

As the temperature reaches 0k, the direction of neighboring magnetic moments should perfectly reverse making the magnetic susceptibility zero. In the other hand, when the temperature is over the Néel temperature T_N, the thermal motion will break the long-range order of antiferromagnet and become paramagnetic [7] (Fig.1.7). Antiferromagnetic follows the Curie-Weiss Law (1.1) with negative Curie constant, which cause by the negative exchange interaction between neighboring electrons [4].

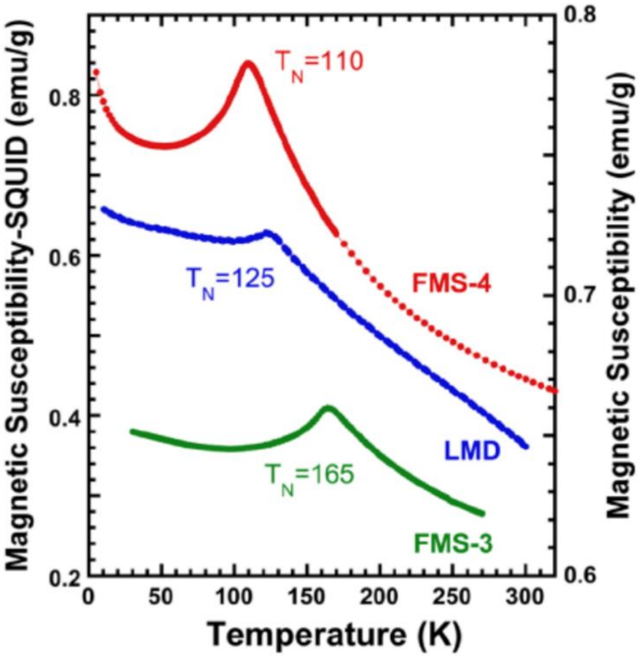

Figure 1. 7: Magnetic susceptibility by temperature to determine T_N of ferromanganese alloys. [7]

1.3 Hall effect

1.3.1 Anomalous Hall effect (AHE)

Late 19th century, American physicist Edwin Herbert Hall discover an effect that is: A cross voltage can be measured when applying a current in FM materials under zero external magnetic field. Since the effect is much different from the original Hall effect, it was later known as anomalous Hall effect (AHE) [8].

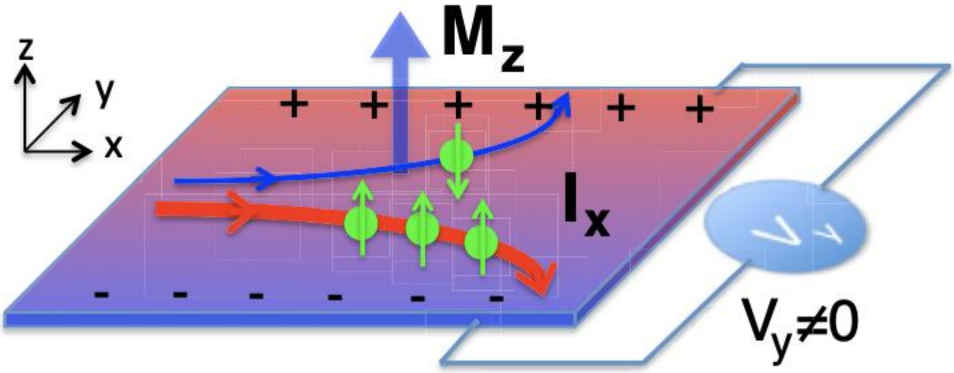

Figure 1. 8: Illustration of anomalous Hall effect. [10]

The effect was shown in Fig.1.8. Due to spin orbit coupling (SOC), the electrons that spin in different direction (up or down) will be deflected into separated ways in FM materials. Since the number of electrons with different spin directions varies, a cross voltage can be generated. The resistance R_{xy} can be expressed as

$$R_{xy} = R_O H_z + R_A m_z \tag{1.2}$$

where R_O is the ordinary Hall effect resistance, H_z is the applied field in z direction, R_A is the AHE resistance and m_z is the z-component of magnetization. We can than measure AHE by probing the direction of m_z since R_O is negligible compared to R_A.

doi:10.6342/NTU202403259

1.3.2 Spin Hall effect (SHE)

Spin Hall effect was first predicted by M. I. Dyakonov and V. I. Perel [11], reintroduced by J. E. Hirsch in 1999 [12] and observed by Y. Kato in 2004 [13]. Since the phenomenon is also SOC driven, like the AHE, when a current flows into SHE material, the electrons in different spin direction will deflect into separated ways (Shown in Fig. 1.9).

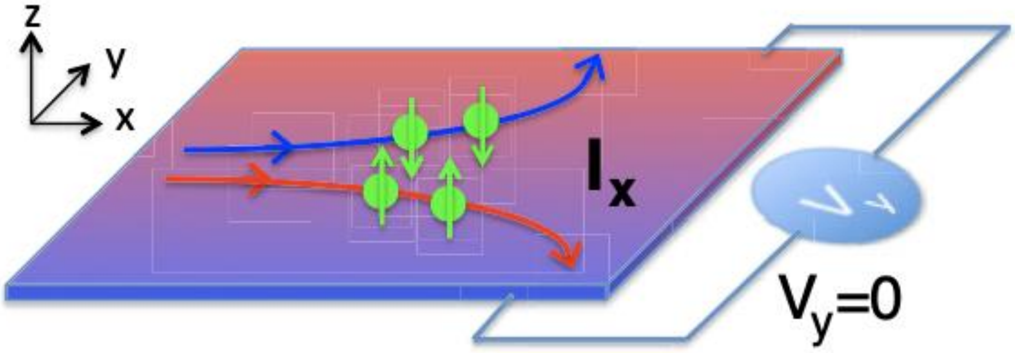

Figure 1. 9: Illustration of spin Hall effect. [10]

Due to the deflection of electrons, a relation between charge current density J_c and generated transverse spin current density J_s can be expressed as

$$J_s = \theta_{SH}(\sigma \times J_c) \tag{1.3}$$

where θ_{SH} represent the spin Hall angle and σ represent the spin polarization. Unlike AHE which is observed in FM materials, SHE was found in nonmagnetic materials and that makes the number of electrons of different spin directions is equal, result in no cross Hall voltage. 5d transition metals (W, Pt, Ta) are promising SHE materials [15][16] because of their strong SOC and good conductivity.

doi:10.6342/NTU202403259

1.3.3 Orbital Hall effect (OHE)

When a current flows through the material, due to the SOC, electrons deflected because of their distinct spin direction. On the other hand, electrons with different orbital angular momentum (OAM) can also be deflected (Fig. 1.10) even without SOC [17], inducing an orbital current perpendicular to the electric field.

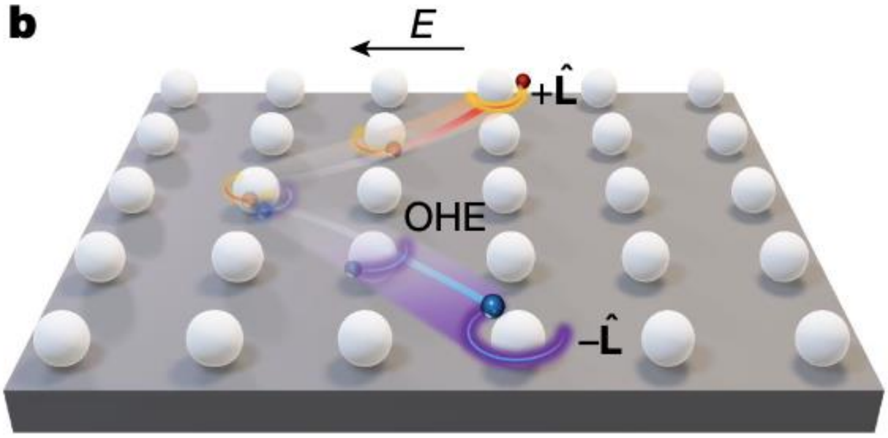

Figure 1. 10: Illustration of orbital Hall effect [17]

OHE has long been theoretical predicted but to observe the direct effect of OHE is challenging since it is hard to separate the contribution from OAM and from spin angular momentum [18]. A group [17] demonstrates a way by using the magneto-optical Kerr effect (MOKE). The MOKE signal confirmed that the OHE-induced moment is larger than the SHE-induced moment. This shows the potential of “orbitronics” and also adding more choices of materials to electrical controlled magnetism since applying the OHE to 3d light transition metals such as Cr [19], Ti [17] and Cu [20] is feasible.

doi:10.6342/NTU202403259

1.4 Magnetic anisotropy

Magnetic anisotropy refers to the directional dependence of a material's magnetic properties. This means that the magnetic behavior of the material, such as how easily it can be magnetized, varies depending on the direction in which an external magnetic field is applied. The easiest direction to magnetize the material is called the easy axis, which is an important factor on the application of magnetic materials.

Magnetic anisotropy was composed of multiple anisotropies in the material including magnetocrystalline anisotropy (MCA), shape anisotropy, strain anisotropy and surface anisotropy. The MCA arises due to the underlying crystal structure of the material. The arrangement of atoms and the spin-orbit interaction within the crystal lattice can make certain directions more favorable for magnetic alignment [21]. Shape anisotropy is cause by demag field which is dependent to the length of the dimension of the object [22]. When applying an external field along the short axis of a thin film, a large demag field will be induced making the magnetization prefer to be in the plane with relatively longer axis. Strain anisotropy changes the preferred magnetization orientation when the material deformed in a dimension that leads to a lattice cell distortion [23]. Surface anisotropy also known as interfacial anisotropy, is induced at the interface of materials. This is origin from the symmetry breaking and may overcome shape anisotropy in some very thin films [24].

1.4.1 In-plane magnetic anisotropy (IMA)

Consider the direction of magnetization easy axis, when the easy axis lies within the x-y plane, an in-plane magnetic anisotropy will be induced. The IMA usually happens on

doi:10.6342/NTU202403259

magnetic single films, because the shape anisotropy is a large component in the total magnetic anisotropy. The effective magnetic anisotropy energy K_{eff} can be express as

$$K_{eff} = K_b + \frac{K_i}{t} - \delta N \frac{{M_S}^2}{2\mu_0} \tag{1.4}$$

where K_b represents the bulk anisotropy energy (~0), K_i is the interfacial anisotropy energy, divided by thickness t, the last term is the shape anisotropy term [24]. As the thickness of FM layer decrease, the effect of shape anisotropy decreases, making K_{eff} increases (Fig. 1. 11). A positive K_{eff} indicates an easy axis that is perpendicular to the x-y plane.

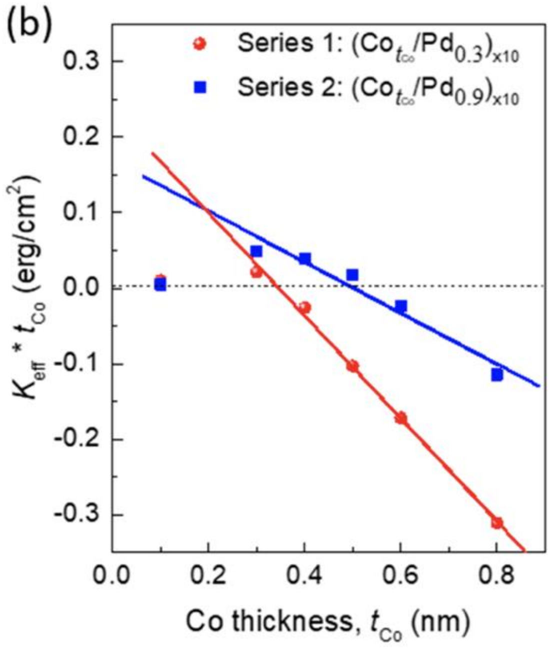

Figure 1. 11: $K_{eff}t_{Co}$ vs Co thickness [25]

1.4.2 Perpendicular magnetic anisotropy (PMA)

Perpendicular magnetic anisotropy (PMA) is the opposite of IMA, which the easy axis stands on the z-direction. The PMA thin film is a much better than IMA ones because of the enhancement of data storage density so it is widely used in MRAM devices, while IMA was used by recording tapes [26].

PMA have two origins majorly: the bulk and the surface. Some bulk properties like MCA and strain magnetic anisotropy built up the bulk PMA. Report [27] said that comparing to interfacial PMA, bulk PMA materials have larger K and better thermal stability, also, the anisotropy will not be diluted when the film grows thicker. Bulk PMA can be induce in transition metal-rare earth alloys (CoTb, CoGd etc.) [28] [29] and $L1_0$-ordered alloys [30].

In contrast to bulk PMA, interfacial PMA was induced by the effect that happens when two different elements meet at the interface. Take Pt/Co for example, the interfacial PMA was induced by intermixing of Pt and Co [31], meaning that the two elements are interdiffused or alloyed during the film deposition. Another commonly used interfacial PMA heterostructure is Ta/CoFeB/MgO. In this case, Ta (5d) has strong SOC so the free electrons hybridize with electrons in CoFeB (3d). Also, Ta atoms are directing to MgO (001) crystal orientation forming a strong MCA. Which indicates that the selection of seeding layer is important in PMA films.

In equation 1.4, when calculating the effective magnetic anisotropy energy K_{eff} in a multi-layer structure, after considering the bulk anisotropy term K_b and shape anisotropy term, we will multiply the interfacial anisotropy term K_i by the number of the interface that induces PMA, take CoFeB/MgO for example (Fig 1. 12), interfacial PMA is induced in free layer and MgO, thus for the double (quad) interfaces' structure, Ki is multiplied by 2(4), and so on.

doi:10.6342/NTU202403259

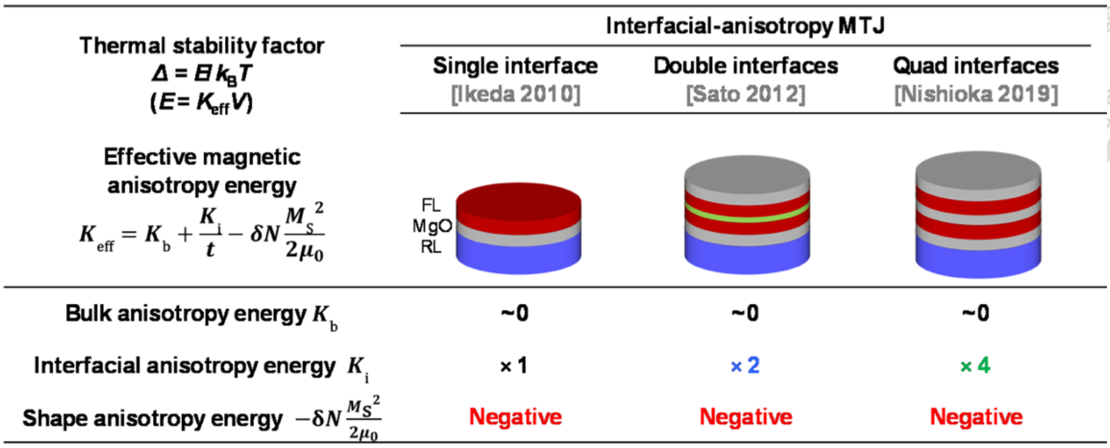

Thermal stability factor $\Delta = E/k_BT$ ($E = K_{eff}V$)	Interfacial-anisotropy MTJ Single interface [Ikeda 2010]	 Double interfaces [Sato 2012]	 Quad interfaces [Nishioka 2019]
Effective magnetic anisotropy energy $K_{eff} = K_b + \frac{K_i}{t} - \delta N \frac{{M_S}^2}{2\mu_0}$	FL MgO RL		
Bulk anisotropy energy K_b	~0	~0	~0
Interfacial anisotropy energy K_i	× 1	× 2	× 4
Shape anisotropy energy $-\delta N \frac{{M_S}^2}{2\mu_0}$	Negative	Negative	Negative

Figure 1. 12: Calculation of K_{eff} in different numbers of interfaces. [24]

1.5 Landau-Lifshitz-Gilbert equation (LLG equation)

The LLG equation was first introduced by Lev Landau and Evgeny Lifshitz in 1935 [33], and later adapt by T. L. Gilbert in 1955 [34]. This differential equation describes the magnetization dynamic in s solid and the relation between magnetization and effective magnetic field. The LLG equation can be expressed as

$$\frac{dM}{dt} = -\gamma^*\left(M \times H_{eff}\right) + \frac{\alpha}{M_s}\left(M \times \frac{dM}{dt}\right) \tag{1.5}$$

where $\gamma^* = \gamma/(1+\alpha^2)$, γ represent the absolute gyromagnetic ratio, α is the Gilbert damping constant, H_{eff} is the effective magnetic field (sum of all existing magnetic fields) and M is the magnetization. In an equilibrium system, the magnetization M should be parallel to the effective field H_{eff}, otherwise, the magnetization will undergo precession around the effective field. The motion is described by the first term called precession term. The second term describes the attenuation of the precession representing the energy dissipation of the system, which is called the damping term.

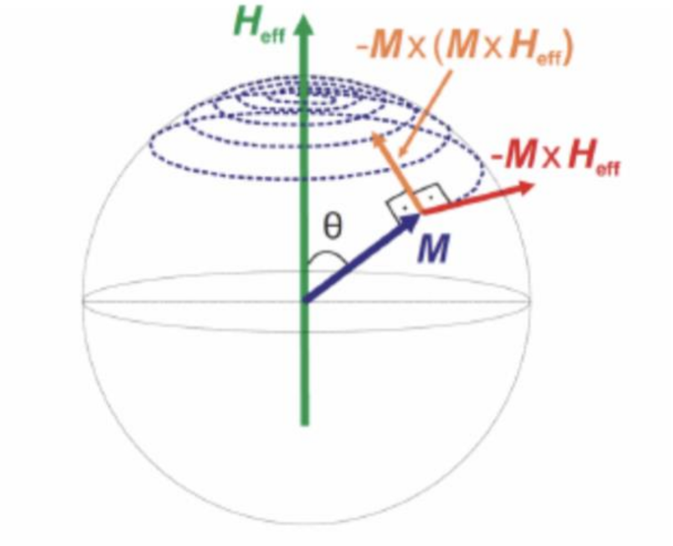

Figure 1. 13: Illustration of the magnetization dynamics under effective field.[35]

1.6 Spin torques

1.6.1 Spin-transfer torque (STT)

J. C. Slonczewski at IBM invented the STT-MRAM in the early 1990s [36]. When the current pass through a FM/NM/FM multilayer, the magnetization of FM layer will be change by the generated STT. By designing the metallic multilayer specifically, the two FM layers can be set in magnetization parallel or antiparallel states. As shown in Fig. 1. 14.

doi:10.6342/NTU202403259

The stability of magnetization for two FM layers is different. The one that its magnetization is easier (harder) to switch is called the free (pinned) layer. When a current flows in the direction from free layer to pinned layer (Fig 1.14a), the electrons will pass pinned layer first and will be spin-polarized by M_{pinned} After the electrons passing through the NM layer, due to angular momentum conservation, the polarized electrons will give the free layer M_{free} a torque $M_{free} \times (M_{free} \times M_{pinned})$, twisting the magnetization to the same direction as M_{pinned}. This makes two FM layers in a parallel state that has lower resistance. To switching the system to antiparallel, current will then be injected from pinned layer to free layer (Fig 1.14b). The magnetization of free layer M_{free} also polarizes electrons, however, when the polarized electron reaches pinned layer, it is not able to switch M_{pinned} since the material was set to have strong anisotropy. Thus, the electrons will be reflected to free layer with a torque $M_{free} \times (M_{free} \times -M_{pinned})$, switching M_{free} in opposite direction. In the antiparallel state, the resistance of the system is higher.

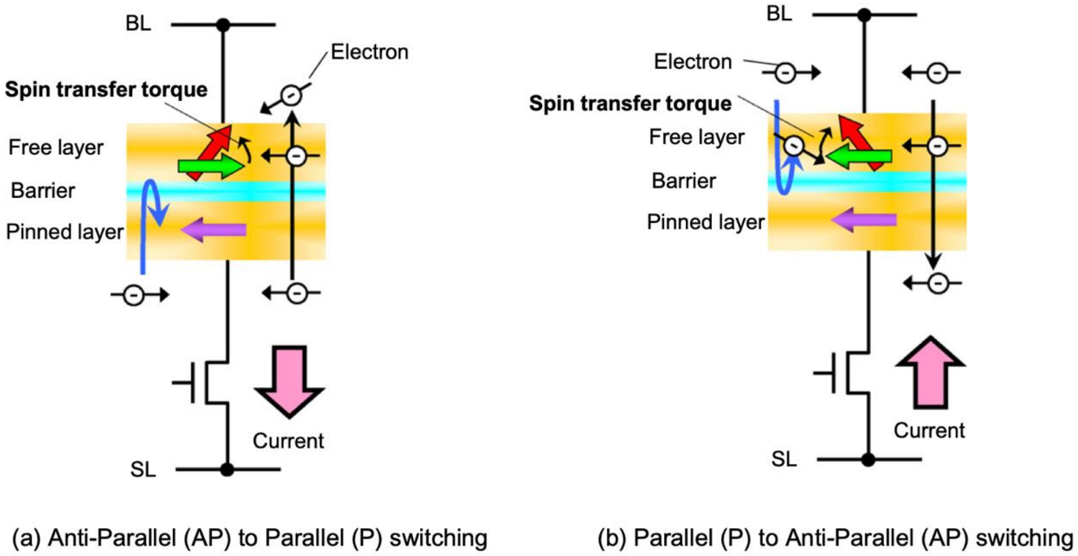

(a) Anti-Parallel (AP) to Parallel (P) switching (b) Parallel (P) to Anti-Parallel (AP) switching

Figure 1. 14: STT-MRAM switching between parallel and antiparallel state. [37]

doi:10.6342/NTU202403259

To calculate the magnetization dynamics in STT-MRAM, a Slonczewski spin transfer torque term is added in LLG equation, the LLGS equation with normalized magnetization m can be expressed as

$$\frac{dm}{dt} = -\gamma\left(m \times H_{eff}\right) + \alpha\left(m \times \frac{dm}{dt}\right) + \tau_{DL}\left(m \times (m \times \sigma)\right) + \tau_{FL}(m \times \sigma) \tag{1.6}$$

where σ represents the spin polarization, τ_{DL} and τ_{FL} represent damping like STT term and field like STT term, respectively. Since the cross product $m \times \sigma$ decides the direction of τ_{DL}, the angle between m and σ is important. If they are in parallel orientation, τ_{DL} will enhance the damping. On the other hand, the damping abates when they are antiparallel. τ_{FL} compared to τ_{DL}, is relatively small which can be negligible.

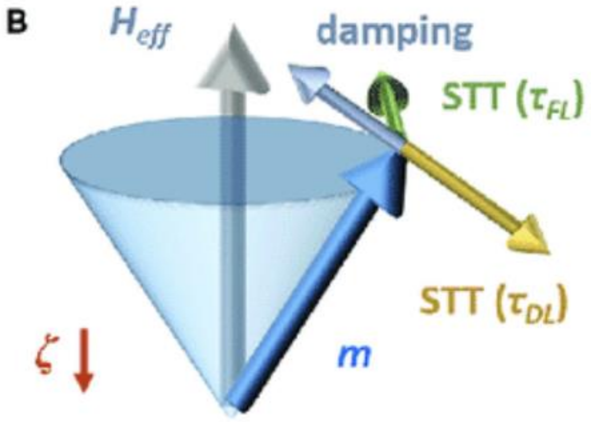

Figure 1. 15: Illustration of field like STT and damping like STT. [38]

doi:10.6342/NTU202403259

1.6.2 Spin-orbit torque (SOT)

As former mentioned, when the current flows in the NM layer along x direction, the SHE induces a transverse spin current with spin polarization along the y direction. When the current flows along z direction, the spins will be injected into the FM layer, exerting a torque on the magnetization of FM, this is called the SOT (Fig 1.16). The spin current J_s corresponded to the input charge current $J_c$can be described as

$$J_s = \theta_{SH} \frac{\hbar}{2e} J_c \times \sigma \tag{1.7}$$

where θ_{SH} represents the spin Hall angle [39].

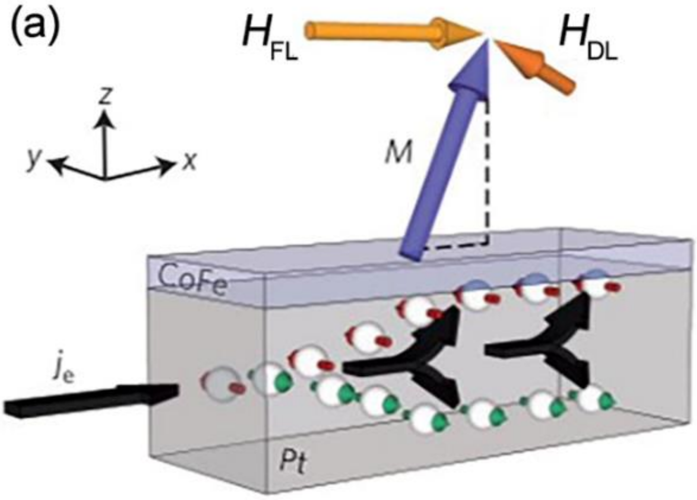

Figure 1. 16: Illustration of SOT in Pt/CoFe bilayer. [39]

Another mechanism of SOT other than SHE is the Rashba effect, which was discovered by Emmanuel Rashba in 1959 [40]. Rashba effect takes place in a system lacking inversion symmetry. The disruption of inversion symmetry can result either from the interface of a bilayer or within the crystal structure. When a charge current is applied, it causes an asymmetric distribution of electrons in k-space (Fig 1. 17), which generates an effective field and induces a nonequilibrium spin density perpendicular to the direction

doi:10.6342/NTU202403259

of the current [39]. This means that if we want to isolate the influence of SHE on SOT, we can design symmetrical structures to minimize the generation of the Rashba effect as much as possible.

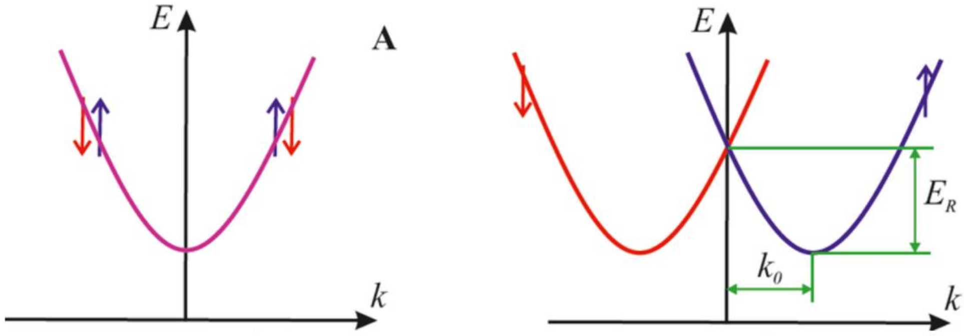

Figure 1. 17: Wave function with (A) and without (B) Rashba spin splitting. [41]

The SOT can also be classified into field-like SOT and damping-like SOT, as shown in Figure 1.18. Unlike the STT scenario, the damping-like SOT can only pull the magnetization toward the x direction. To reach deterministic magnetization switching, an external in-plane field is necessary, which is one of the major challenges in manufacturing SOT devices.

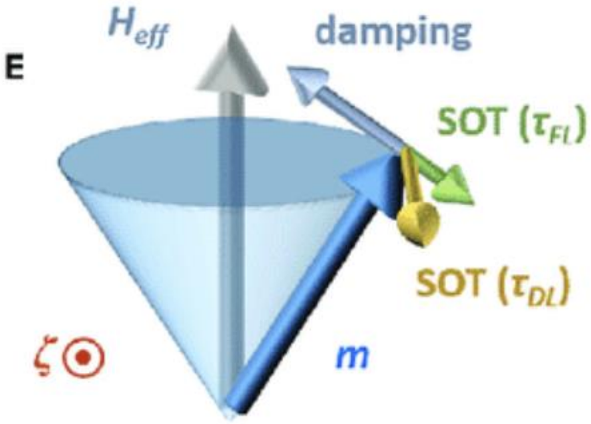

Figure 1. 18: Illustration of field like SOT and damping like SOT. [38]

doi:10.6342/NTU202403259

1.7 Field free switching

1.7.1 Idea of field free switching

Consider two states, 1 and 2, where the magnetization of state 1(2) is in +z(-z) direction. To achieve deterministic switching is to switch from state 1 to 2, however, if state 1 is stable, state 2 should be stable as well. Since it is hard to switch from two equally stable state, one of them must be slightly unstable than another one. Therefore, symmetry breaking is necessary to fulfill deterministic switching. By applying a magnetic field toward the -x direction at state 1, deterministic switching can be reach since the applied field have to be in +x direction to remain the symmetry (Fig 1.19). For more practical uses, deterministic switching must happen without the extra field, this is called Field free switching.

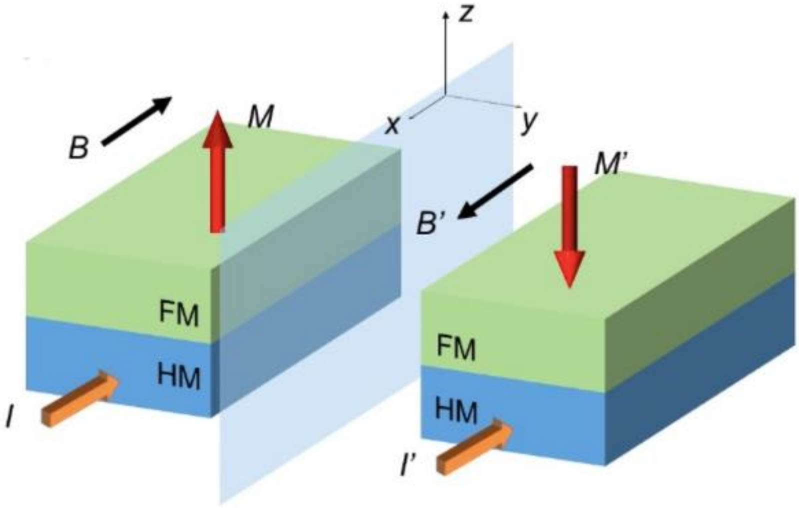

Figure 1. 19: Equally stable state 1 and 2 under applied field in x-direction. [39]

doi:10.6342/NTU202403259

1.7.2 Ways to reach field free switching

Various way can be used to fulfill field free switching by breaking the symmetry in different aspects. One of the common ways is lateral structural symmetry breaking. By wedging the FM (CoFeB[44]) or NM (Ta[42], Pt[43]) layer or a thin wedge light metal insertion [45], the symmetry in y-direction is broken, which the current will thus induces an effective field in z-direction. Since the induced field depends on the direction of current, certain direction of current will have a favor state, therefor, deterministic switching can be reach.

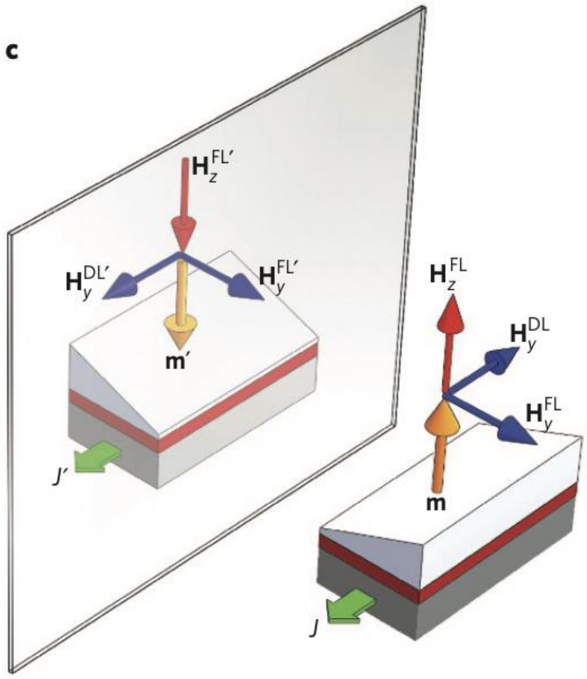

Figure 1. 20: Mirror symmetry of y-direction symmetry breaking. [42]

Another way to fulfill field free switching is though interlayer coupling. For example, an AFM layer is placed above the FM layer forming an AFM/FM interface. The exchange bias at the interface plays the role off an in-plane field to break the symmetry. After field annealing [46] or sputtering under an in-situ field[47], the perpendicularly magnetized FM layer will tilted by the exchange bias and field free switching can then be reach.

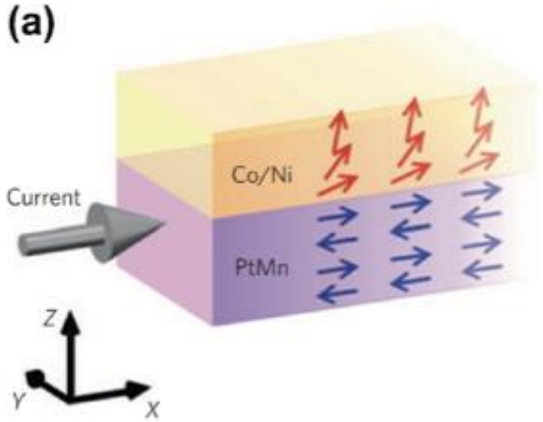

Figure 1. 21: Illustration of exchange bias in Co/Ni/PtMn system. [46]

Other than mirror symmetry, breaking the chiral symmetry is another aspect to fulfill FSS, which is usually done by introducing Dzyaloshinskii-Moriya interaction (DMI) [48]. DMI is an exchange interaction between neighboring spins S_i and S_j, which its Hamiltonian H_{ij} can be describe as

$$H_{ij} = D_{ij} \cdot (S_i \times S_j) \tag{1.8}$$

where D_{ij} represents the DMI tensor. The DMI will lead to chiral spin texture (Fig 1.22), with certain current direction and a given DMI, a specific texture is preferred due to the lower DMI energy. Therefore, the magnetization direction is decided by current and FSS can be fulfilled.

doi:10.6342/NTU202403259

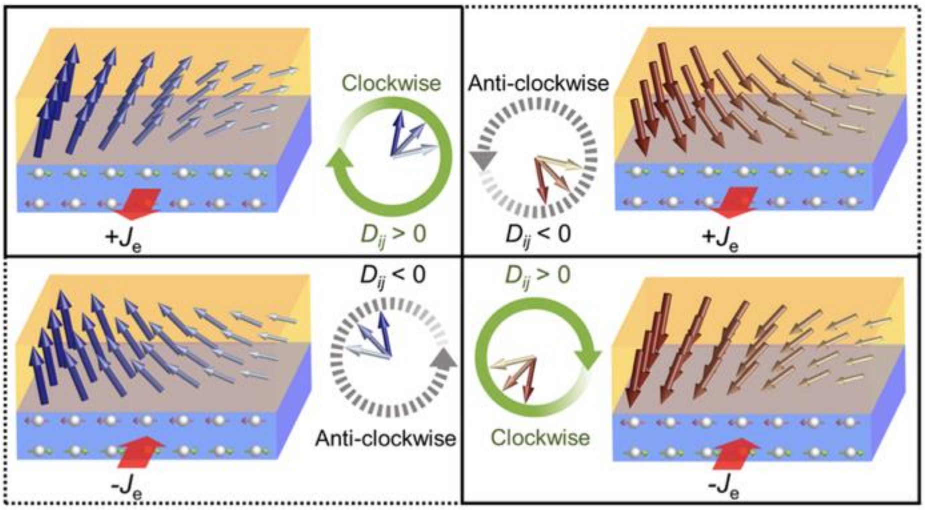

.

Figure 1. 22: Four possible non-colinear spin textures given by DMI.[46]

1.8 Motivation of this work

Compared to STT-MRAM which rely on spin polarization current, SOT-MRAM utilizes SOT to switch the magnetization, giving it various of advantages such as faster writing speed, lower energy consumption, lower data loss, longer lifespan etc... For SOT-MRAM, finding a way to fulfill deterministic current induced magnetization switching is crucial in industrial applications[49]. Field free switching can be realized by several ways including lateral symmetry breaking (wedge), chiral symmetry breaking (DMI) and interlayer coupling (exchange bias). In this work, I studied the effect and evaluate the switching ratio when wedging different layer in Ta/Pt/Co/Pt/Ta PMA system, including combination of wedge layers with different directions. The anneal process is also conduct on the wedge sample to observe the enhancement of SOT.

Chapter 2 Experiments

2.1 Hall bar fabrication

2.1.1 Photolithography

To facilitate electrical measurements of the magnetic thin film, we have fabricated the device in the shape of a double cross Hall bar. First, the substrate is baked to remove the moisture at 373K. Then the positive photoresist is carefully dripped on the wafer and put on the spin coater to form a uniform photoresist film. The photoresist should be retreat to room temperature before use. After spin coating, the wafer is baked again to dry out the solvent and release the stress of the film. UV exposure will increase the dissolution rate of the positive photoresist in the developer (TMAH). After the exposed photoresist is washed off by TMAH and DI water, the pattern of mask will be transfer to photoresist on the substrate.

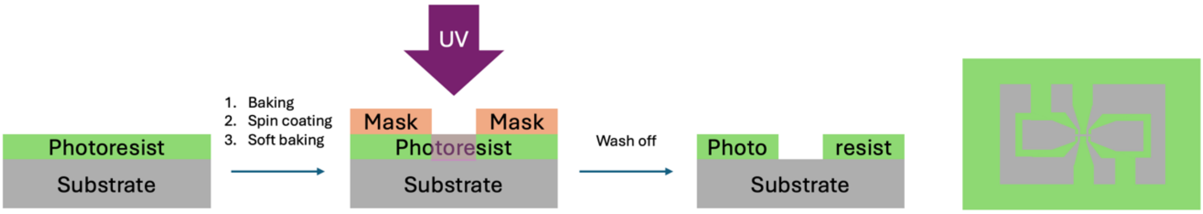

Figure 2. 1: Process of photolithography of the Hall bar pattern.

2.1.2 Magnetron sputtering

Magnetron sputtering is a common vacuum coating technique based on Physical Vapor Deposition (PVD), widely used in the manufacture of semiconductors, optical components, and various surface coatings. First, the substrate with Hall bar pattern are placed in a vacuum chamber. The air in the chamber is evacuated to reduce impurities and gas molecules, enhancing the quality and adhesion of the coating. After the pressure decrease to $1*10^{-7}$, Argon gas is introduced into the vacuum chamber to generate ions. A voltage difference is created between the target material and the substrate, forming plasma. In the plasma, gas molecules are ionized into positive ions and free electrons by electron impact. A strong magnetic field is configured around the target material to control the motion of electrons, increasing the collision probability of ions and electrons on the target surface, thereby enhancing the deposition rate. The positive ions are accelerated by the electric field towards the negatively charged target material and bombard it. This high-energy bombardment causes atoms from the target material's surface to be ejected (sputtered), which then fly towards the substrate and condense on its surface to form a film. By controlling parameters such as sputtering time, power, and gas pressure, the film's thickness and properties can be precisely controlled. After sputtering, the substate is soaked in toluene and vibrate in ultrasonic cleaner to remove the photoresist.

In this thesis, all the materials are deposited on the thermally oxidized Si wafer at room temperature, with DC power 30W and the working pressure of argon is 3 mTorr. The substrate holder rotates at 10 rpm and the rotation is turn off when depositing wedge layers.

doi:10.6342/NTU202403259

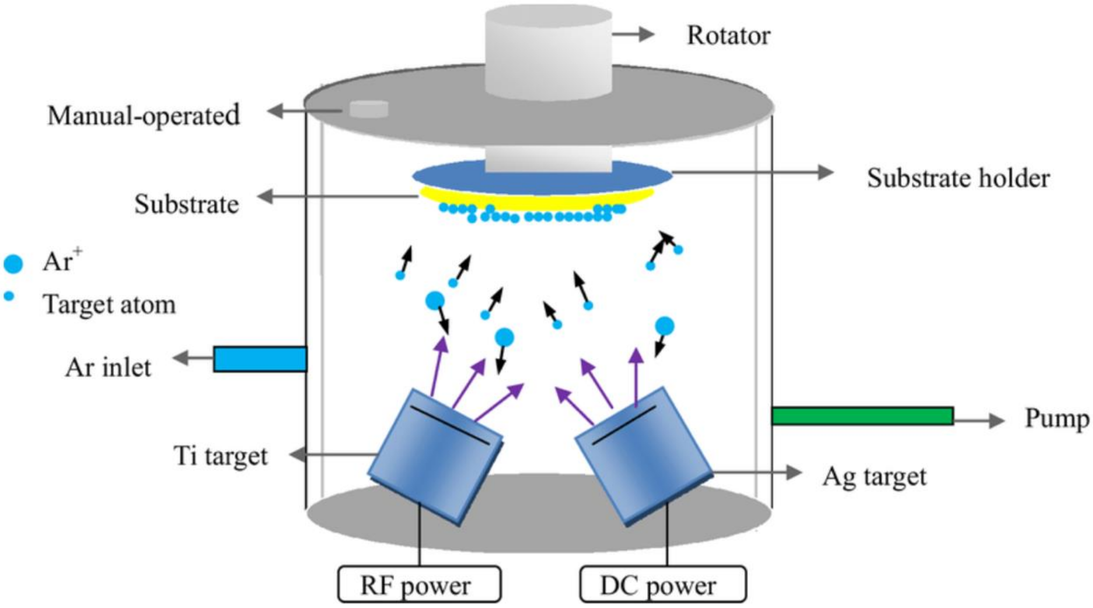

Figure 2. 2: Illustration of magnetron sputtering. [50]

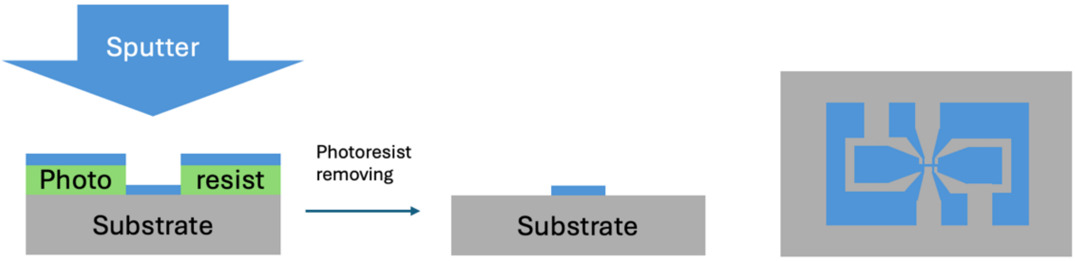

Figure 2. 3: Lift off process.

2.2 Measurement methods

2.2.1 Loop shift measurement

Loop shift measurement is used to extract the damping like torque efficiency ξ_{DL} and the DMI effective field H_{DMI} in PMA films. In FM layer, Néel domain wall (DW) separates magnetic moment in different direction, while DMI stabilizing it. The SOT exerted by SHE will effect on the DW moment and become an effective field perpendicular to the PMA film (H_{eff}^{z}). Without an in-plane field H_x, the moments will not tilt in certain x direction, result in opposite direction of neighboring DW moments, which the DWs move simultaneously so the domain does not expand (Fig 2. 4a). On the contrary, the moments will be tilted in same x direction when H_x is applied and the H_{eff}^{z} will point in same direction, the domain will then be expanded (Fig 2. 4b).

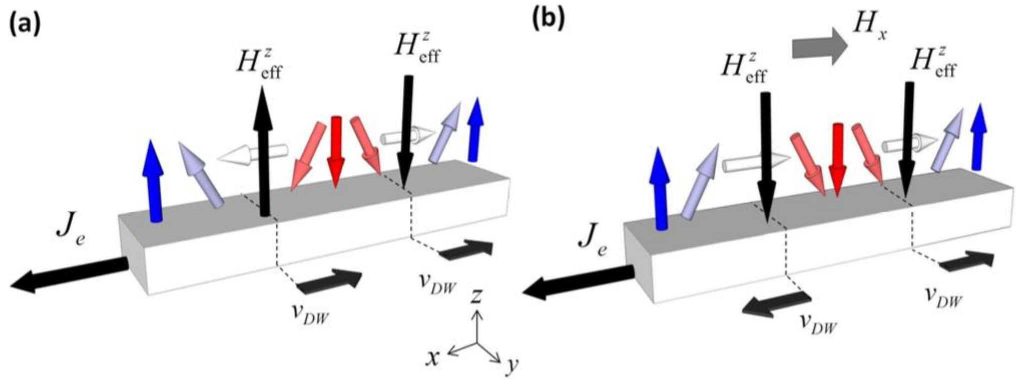

Figure 2. 4: Illustration of Néel DW motion of a PMA heterostructure (a)with and (b)without H_x. [51]

The experiment setup is shown in Fig. 2. 5a. A dc current I_{DC} and an in plane magnetic field H_x is applied along the x direction. Sweeping the out of plane field H_z and measuring the cross voltage will result in a hysteresis loop as shown in Fig. 2. 5b. By applying different I_{DC}, the hysteresis loop will “shift” and the dependence of H_{eff}^{z} and I_{DC} can be extracted as shown in Fig. 2. 5c. When larger H_x is applied, the slope H_{eff}^{z}/I_{DC} will eventually saturate when H_x overcome DMI field, and the value is related to the SOT efficiency χ_{SHE}, as shown in Fig. 2. 5d.

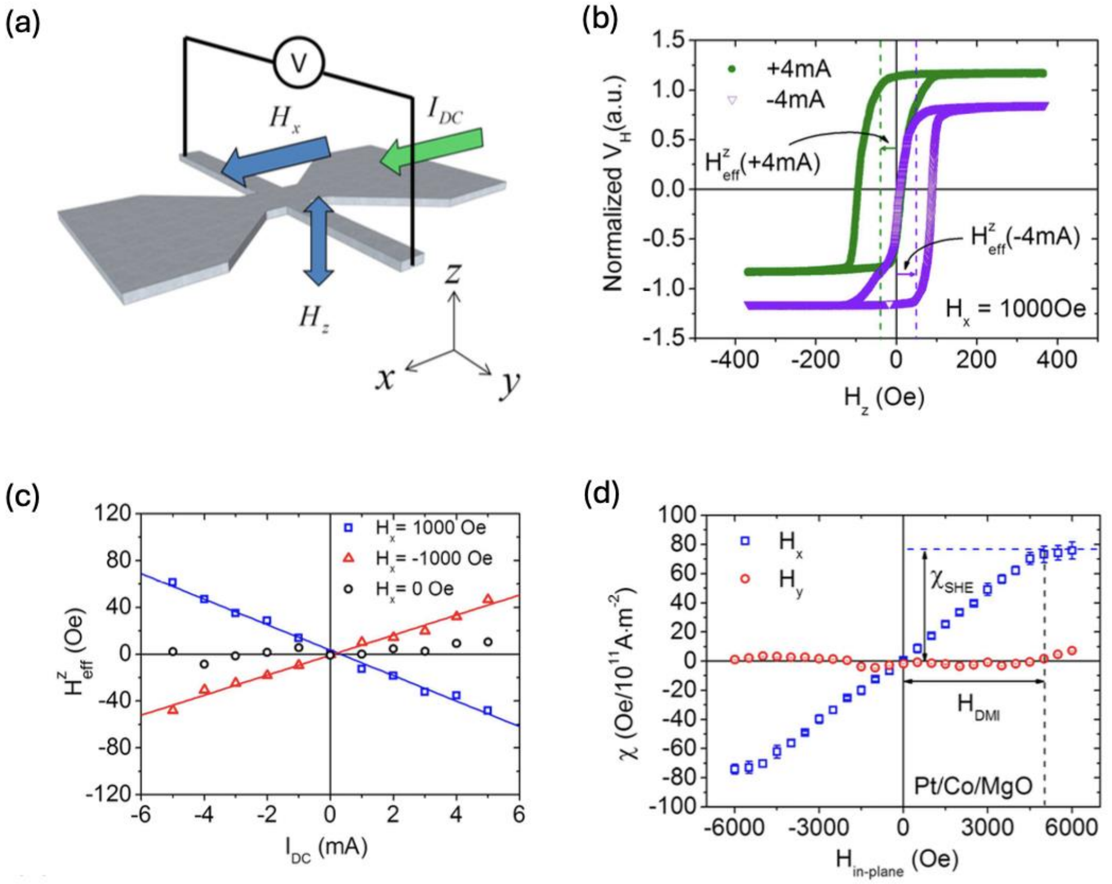

Figure 2. 5: (a) Setup of hysteresis loop shift measurement. (b) Hysteresis loop of Pt(4)/CoFeB(1)/MgO(2) sample with I_{DC} = ±4 mA and H_x = 1000 Oe. (c) H_{eff}^z vs I_{DC} under different H_x of Pt(4)/CoFeB(1)/MgO(2) sample. (d) χ as a function of applied H_x for Pt(4)/Co(1)/MgO(2). [51]

2.2.2 Current-induced SOT field-free switching measurement

The experiment setup is same as the loop shift measurement (Fig. 2. 5a) but the applied field provided by 5204 projector vector field magnet from GMW associates [52], H_x and H_z, are removed. The write current is provided by Keithley 2400 sourcemeter and the Hall voltage is measure by Keithley 2000 multimeter. By sweeping the write current I_{write}, current induced SOT will switch the magnetization in FM layer, forming a hysteresis loop as shown in Fig. 2. 6. From the loop we can obtain the critical switching current which is the minimum I_{write} to switch the magnetization and ΔR which is difference of resistance between opposite magnetizations. The switching ratio can be calculated as

$$\frac{\Delta R_{field\ free}}{\Delta R_{field}} \times 100\% \qquad (2.1)$$

which represents the ability and efficiency of achieving magnetic state transitions without the assistance of an external magnetic field.

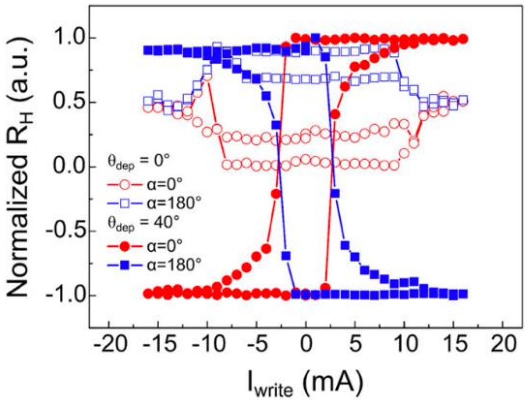

Figure 2. 6: Representative field-free switching loops for Pt/Co/Pt wedge system. [43]

Chapter 3 Result

Due to the perpendicular magnetization direction, magnetic heterostructure with PMA is considered to have multiple advantages such as higher stability to heat, larger storage density and scalability. Also, as former mentioned, symmetry breaking is critical for fulfilling field free switching in SOT-MRAM. There are various ways to break the symmetry and a simple reach is wedge deposition in magnetic heterostructure, which has low fabrication difficulty. Therefore, a simple magnetic heterostructure with PMA, Ta(1)/Pt(2)/Co(0.8)/Pt(1)/Ta(2), is chosen, as shown in Fig. 3. 1. Inspired by Hu's work [43] which investigate the relation between tilted anisotropy and wedge Pt buffer layer, we further dig in the influence of wedging every layer from seeding layer to capping layer. We also discovery the probability to combine multiple wedge layers with different directions.

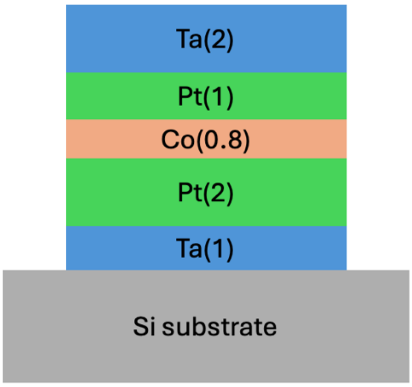

Figure 3. 1: Schematic illustration of the Ta/Pt/Co/Pt/Ta layer stack.

doi:10.6342/NTU202403259

3.1 SOT characterization of control sample

First, current-induced SOT-driven magnetization switching measurement in utilize to characterize the basic properties of SOT switching of the control sample with full rotation depositing (No wedge). The AH loop measurement under I_{DC} = 1 mA, H_z sweeping between ±300 Oe is shown in Fig. 3. 2a where Hall resistance R_H=5.3 Ohm and H_C= 114 Oe. The relation between H^z_{eff} and I_{DC} under H_x=±500 Oe is shown in Fig. 3. 2b, clearly showing a linear behavior. Relation between the slope H^z_{eff}/I_{DC} and in-plane field H_x is shown in Fig. 3. 2c, indicate that the loop shifts in opposite direction when positive and negative H_x is applied. The saturation value of the slope H^z_{eff}/I_{DC} =8.3 Oe/mA is extracted when H_x reaches 600Oe, which pointed out the overcoming of H_{DMI} by the applied field.

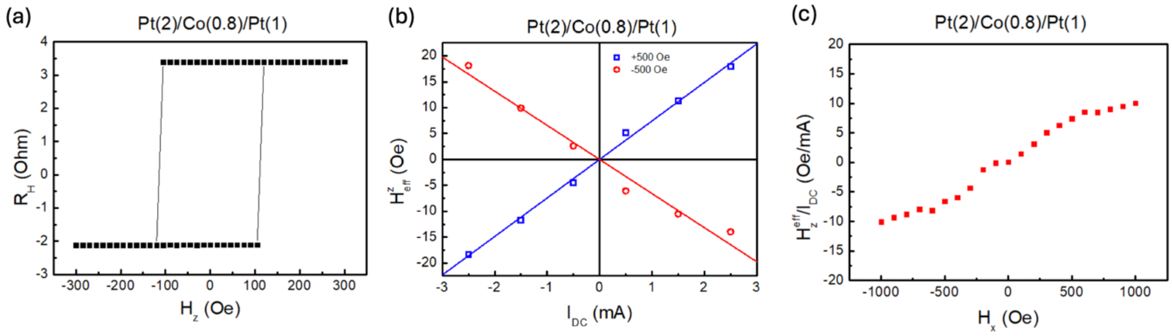

Figure 3. 2: SOT characterization of Ta(1)/Pt(2)/Co(0.8)/Pt(1)/Ta(2) control sample. (a) AH loop result. (b) H^z_{eff} as a function of I_{DC} under H_x=±500 Oe. (c) H^z_{eff}/I_{DC} as a function of H_x.

The wedge sample is then fabricated by magnetron sputtering, since the plane normal of target and substrate holder is not parallel, stopping the rotation of substrate holder will result in an oblique deposited film. The wedge deposition direction is perpendicular to the current in order to break the symmetry. The AH loops of different wedge layers are

doi:10.6342/NTU202403259

measured and the coercive field H_C and ΔR_H is shown in Fig 3. 3, indicates that wedging a certain layer does not change the loop properties significantly.

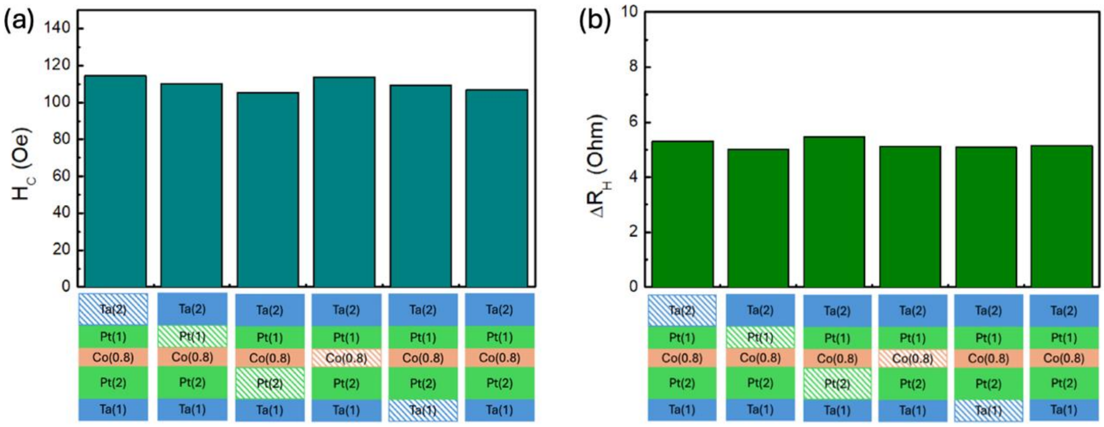

Figure 3. 3: (a) H_C comparison of different wedge layers. (b) ΔR_H comparison of different wedge layers.

3.2 Current-induced SOT field-free switching of single wedge layer

In order to demonstrate the field free switching behavior, the experiment was conducted in an environment without any potentially impactful external magnetic field. The setup of the experiment is illustrated in Fig. 3. 4. Note that the yellow arrow indicates the wedge direction from near to far. The result of current induced SOT field free switching of different wedge layers is shown in Fig. 3. 5. For wedge Pt samples, both upper and bottom Pt wedge performs clear switching loop in opposite writing current direction, manifested a deterministic field free switching behavior with a ~50% switching ratio for bottom Pt wedge and ~65% switching ratio for upper Pt wedge. Both have a critical switching current ~11mA. For wedge seeding Ta, the switching loop is also clear and perform deterministic field free switching at a switching ratio ~50%, however, compared to wedge Pt samples, the critical switching current is almost twice as high which was as expected since Ta layer is distanced from the Pt/Co interface. As for control sample, wedge Co and wedge capping Ta sample, no field free switching is observed since the switching ratio is almost 0 and cannot accomplish deterministic switching.

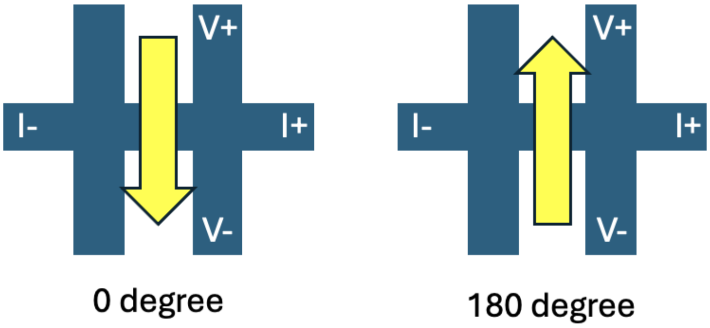

Figure 3. 4: Experimental setup of current-induced SOT field-free switching measurement.

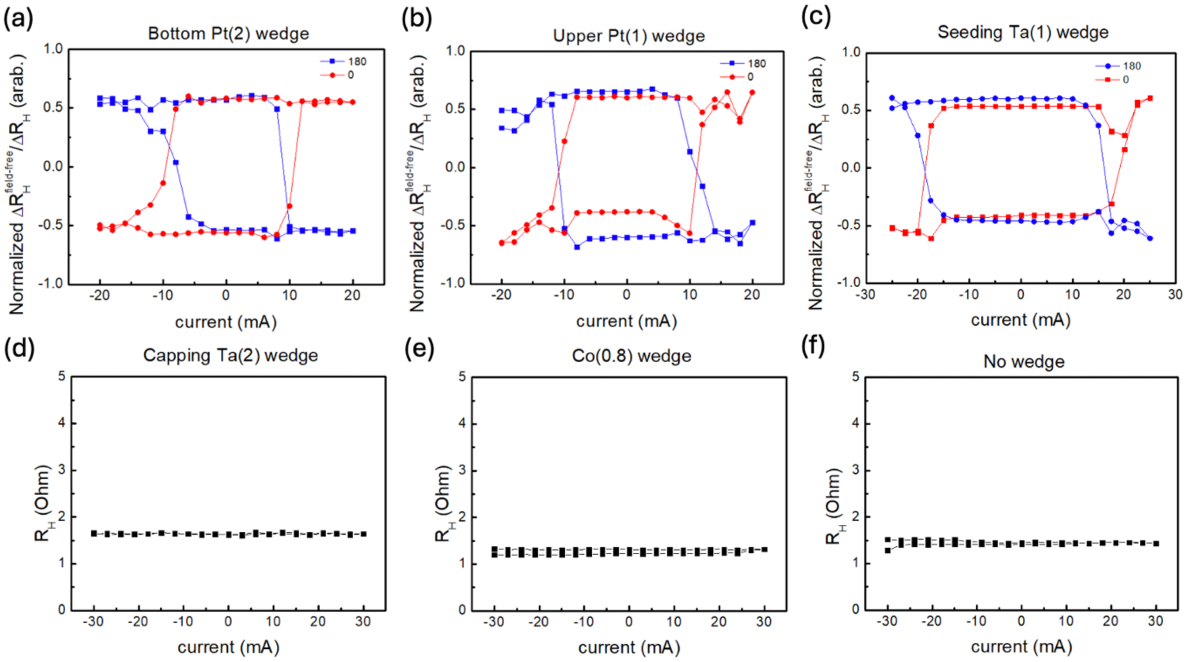

Figure 3. 5: Representative current induced field free SOT switching loops for (a)wedge bottom Pt layer, (b)wedge upper Pt layer and (c)wedge seeding Ta layer samples. Field free switching measurements for (d)wedge capping Ta, (e)wedge Co and (f)control sample.

3.3 Tilted PMA characterizing of single wedge layer

To observe the miniature deviation of the perpendicular magnetic easy axis, fixed current AHE loop shift measurement with different in plane magnetic field direction is applied. If the magnetic anisotropy easy axis is ideally perpendicular to the film, the AH loop will not shift since the applied in plane field is unable to project onto the vertical easy axis. In the other hand, the slightly tilted easy axis will reflect the in plane magnetic field resulting in loop shifting. To avoid the effect of Joule heating, applied current for AHE is set to 0.1mA. To find out the direction of tilted anisotropy precisely, the azimuthal angle ϕ_{ani} and polar angle θ_{ani} must be extracted. We can calculate from the loop shift results, the total magnetic field on the easy axis H_{ea} is the sum of the projection of z direction field H_Z on the easy axis and the projection of in plane field H_{IP} on the easy axis [43]. That is

$$H_{ea} = H_z cos\theta_{ani} + H_{IP}\cos(\theta_{ani} - \phi_H)\, sin\theta_{ani} \qquad (3.1)$$

By AHE loop we define the shift of loop center ΔH_{SW} as

$$\Delta H_{SW} \equiv \frac{(H_{SW}^{down\ to\ up} + H_{SW}^{up\ to\ down})}{2} \qquad (3.2)$$

On the easy axis, the magnitude of magnetic field required to shift from up to down and from down to up should be equal, therefore, loop center shift ΔH_{SW} should be in proportion to the in plane magnetic field H_{IP}, the relation can be organized into

$$\frac{\Delta H_{SW}}{H_{IP}} \equiv \frac{\left(H_z^{down\ to\ up} + H_z^{up\ to\ down}\right)}{2H_{IP}} \qquad (3.3)$$
$$= -\cos(\phi_{ani} - \phi_H)\, tan\theta_{ani}$$

The linear relation between ΔH_{SW} and H_{IP} with respect to different in plane field angle is shown in Fig. 3. 6. For the control sample without wedge deposition, H_{IP} with 90° lies along ΔH_{SW} = 0 Oe, indicate that no shift of out of plane loop which manifest a vertical magnetic easy axis. In contrast, for wedge seeding Ta, wedge bottom and upper Pt samples which present deterministic field free switching clearly perform the out of plane loop shifting, indicating the presence of a tilted magnetic easy axis. By fitting equation 3.3 and the slope $\frac{\Delta H_{SW}}{H_{IP}}$, as shown in Fig. 3. 7, ϕ_{ani} and θ_{ani} of the tilted PMA of different wedge layers are extracted. The comparison of ϕ_{ani} and θ_{ani} with different wedge layers is shown in Fig. 3. 8. Note that the direction of tilted magnetic anisotropy is similar for both upper and bottom Pt wedge samples, with ϕ_{ani} ~ 60° and θ_{ani} ~15°. In Hu's work[43], ϕ_{ani} is measured to increase with deposition angle of Pt and could eventually reach 80°. Since we did not adjust the deposition angle in this experiment, the result is reasonable. As for seeding Ta wedge sample, ϕ_{ani} is almost 90° which is thought to be wedge deposited ideally. The θ_{ani} of wedge Ta sample is also the largest of all (~20°). We assume that since Ta layer is the first to be deposited, it will tilt the structure of entire film and the magnetic anisotropy.

doi:10.6342/NTU202403259

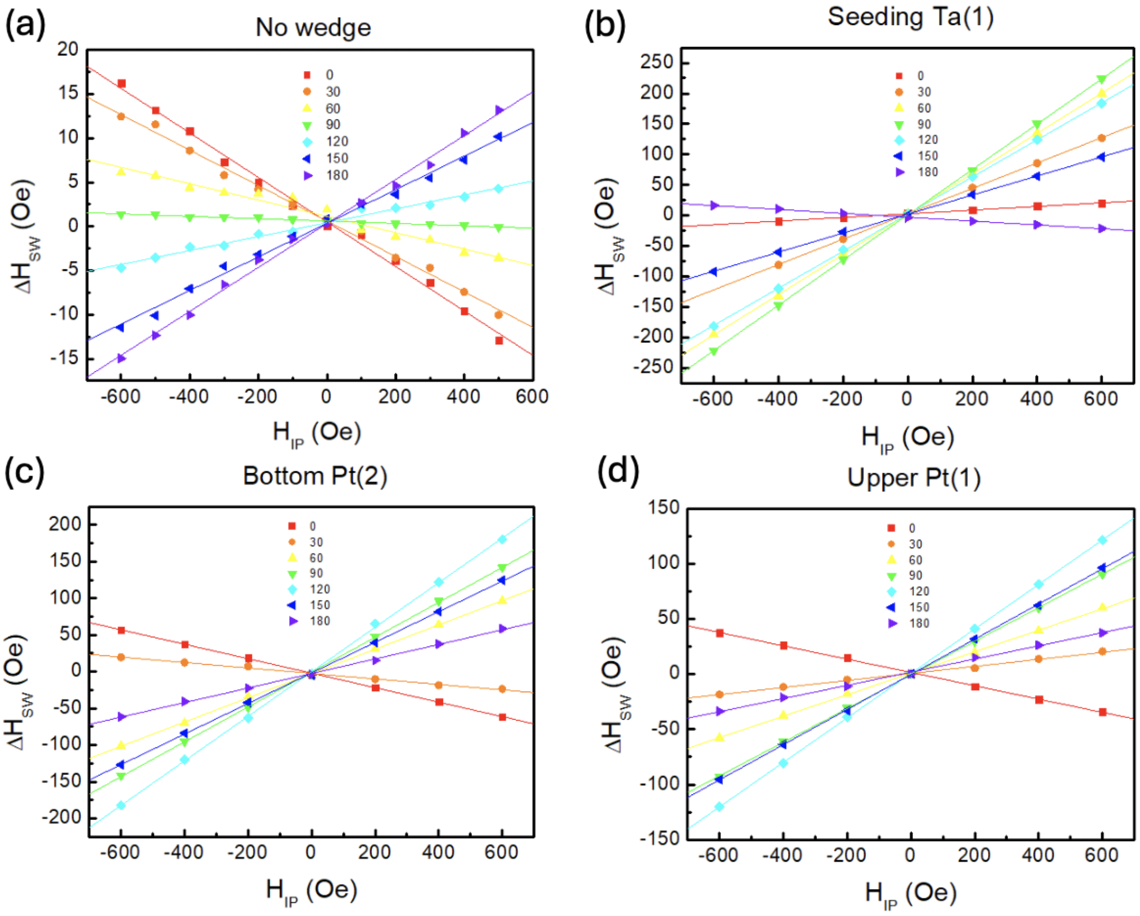

Figure 3. 6: Linear relation between switching field ΔH_{SW} and in plane magnetic field H_{IP} scanning in different in plane field angle of (a)control sample, (b)wedge seeding Ta layer, (c)wedge bottom Pt and (d)wedge upper Pt.

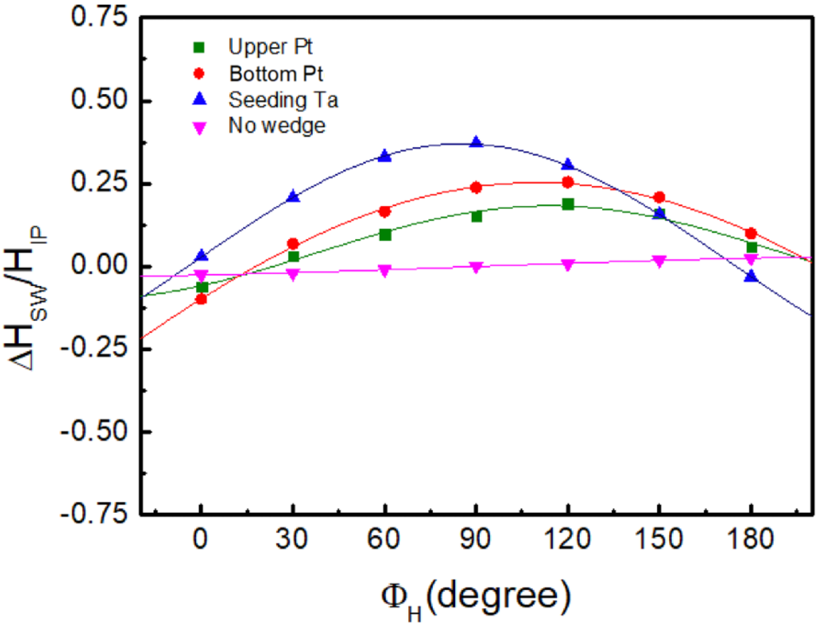

Figure 3. 7: Sinusoidal relation between $\frac{\Delta H_{SW}}{H_{IP}}$ and ϕ_H of upper Pt wedge, bottom Pt wedge Seeding Ta wedge and control sample, fitting by equation 3.3.

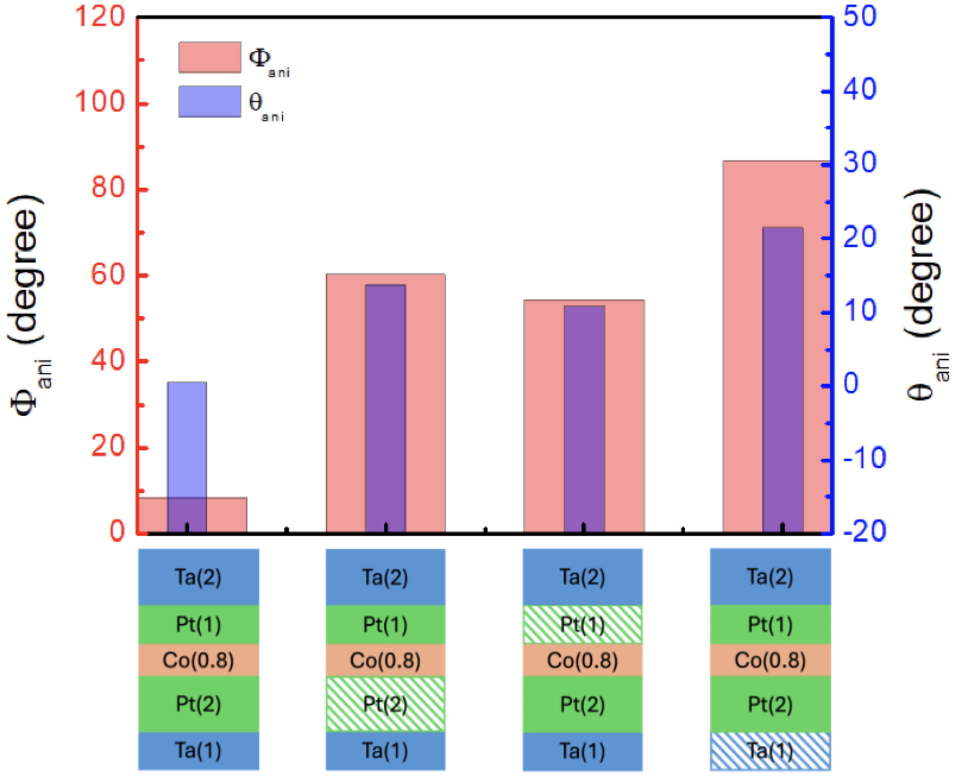

Figure 3. 8: Comparison of the azimuthal ϕ_{ani} and polar angle θ_{ani} of tilted anisotropy of upper Pt wedge, bottom Pt wedge, Seeding Ta wedge and control sample.

3.4 Parallel and antiparallel wedge Pt layer

After the influence of wedging each layer in Ta/Pt/Co/Pt/Ta magnetic heterostructure at once is characterized, inspired by Huang's work in interlayer DMI [53], we further the outcome of combining Pt wedge layers with parallel and antiparallel wedge directions. The schematic illustration of parallel and antiparallel wedge Pt is shown if Fig. 3. 9a, note that the red arrow represents the direction of deposition. The hysteresis loop shift measurement is adopted and the H^{z}_{eff}/I_{DC} with respect to H_X is shown in Fig. 3. 9b. The slightly drop in H^{z}_{eff}/I_{DC} of antiparallel wedge Pt sample might be due to the impurity in fabrication process. Since the rotation of the substrate holder cannot be controlled precisely, the antiparallel sample is taken out of the chamber to rearrange the substrate in order to deposit the upper Pt layer in an opposite direction.

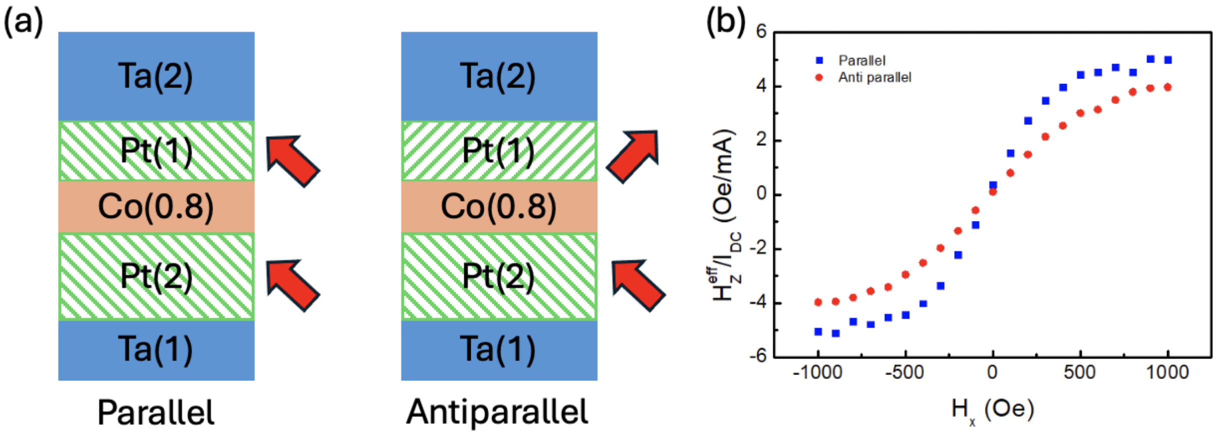

Figure 3. 9: (a) Schematic illustration of parallel and antiparallel wedge Pt magnetic heterostructures. The red arrow is the direction of wedge deposition. (b) H^{z}_{eff}/I_{DC} with respect to H_X f parallel and antiparallel wedge Pt samples.

Current induced SOT field free switching measurement is conducted, and the result is shown in Fig. 3. 10. Both parallel and antiparallel wedge Pt samples perform clear switching loop in opposite writing current directions, indicate a deterministic field free switching. For parallel wedge sample, the field free switching ratio can reach 73% which is small improvement compared to upper Pt wedge. The critical switching current is 5mA, showing a significant 50% reduction to single Pt wedge samples. For antiparallel wedge sample, the critical switching current remains low at 5mA, but the switching ratio decreases to 25%. A noticeable point is that the switching polarity of antiparallel wedge is opposite to parallel wedge and other single wedge Pt samples, which will be explained later.

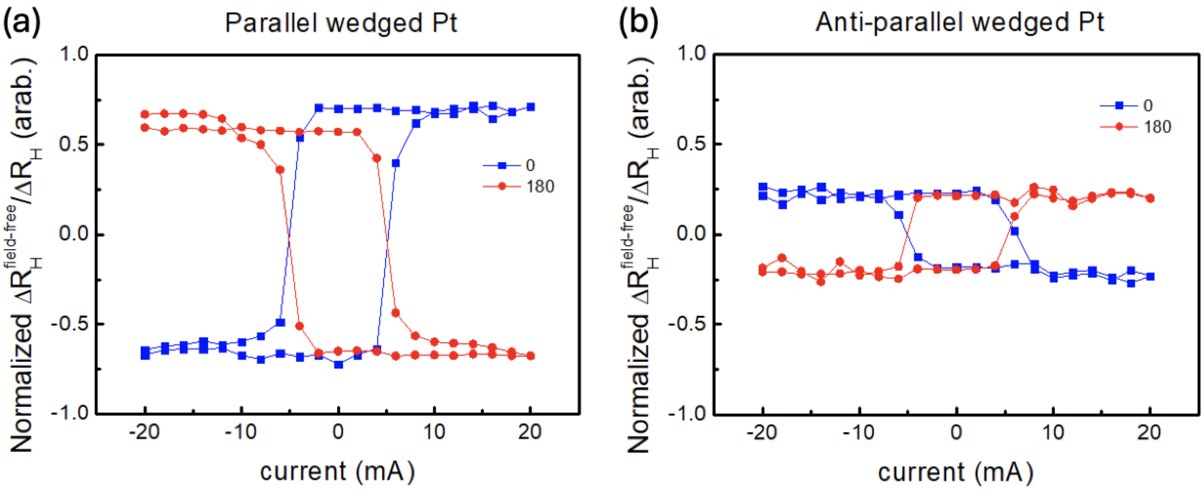

Figure 3. 10: Representative current induced field free SOT switching loops for (a) parallel wedge Pt layers and (b) antiparallel wedge Pt layers.

We further conduct the fixed current loop shift measurement with different in plane magnetic field to characterize the tilted anisotropy of parallel wedge Pt sample. The sinusoidal relation between $\frac{\Delta H_{SW}}{H_{IP}}$ and ϕ_H is shown in Fig. 3. 11, and the comparison of azimuthal ϕ_{ani} and polar angle θ_{ani} is summarized in Fig. 3. 12. Note that ϕ_{ani} is same compared to upper and bottom wedge Pt sample while θ_{ani} is slightly larger which reflect the increment of field free switching ratio. The enhancement of the θ_{ani} is as expected since the tilted magnetic anisotropy is strongly dependent on the crystalline texture, that is, the PMA is form by the Pt (111) texture in Pt/Co and by our result, in

Co/Pt as well [54][55]. Therefore, parallel wedge Pt sample forms the tilted Pt (111) texture at the bottom Pt layer, then, repeat at the upper Pt. Will result in the enhancement of overall tilted texture in Pt/Co/Pt system and the consequent of larger θ_{ani}. In the other hand, the contribution of two upper and bottom Pt wedge layer in tilted texture will compete since they are deposited in opposite direction. The mechanism is illustrated in Fig. 3. 13, note that the iron gray arrow represents the direction of tilted texture, and the purple arrow represents the direction of the tilted magnetic anisotropy. As former mentioned, the switching polarity is opposite for the antiparallel wedge sample. The reason is in the specific situation, the contribution of the upper wedge Pt overcome the bottom Pt, forming a negative polar angle θ_{ani}. The polar angle θ_{ani} is then balanced out by the competence of upper and bottom wedge Pt layers.

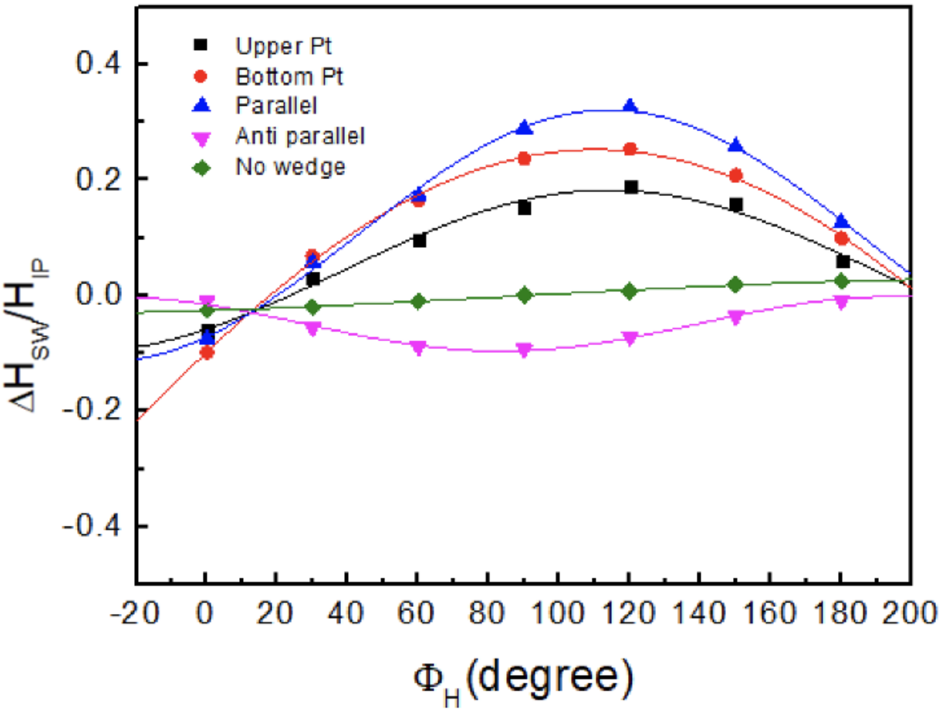

Figure 3. 11: Sinusoidal relation between $\frac{\Delta H_{SW}}{H_{IP}}$ and ϕ_H of no wedge, upper Pt wedge, bottom Pt, parallel wedge Pt and antiparallel Pt sample, fitting by equation 3.3.

doi:10.6342/NTU202403259

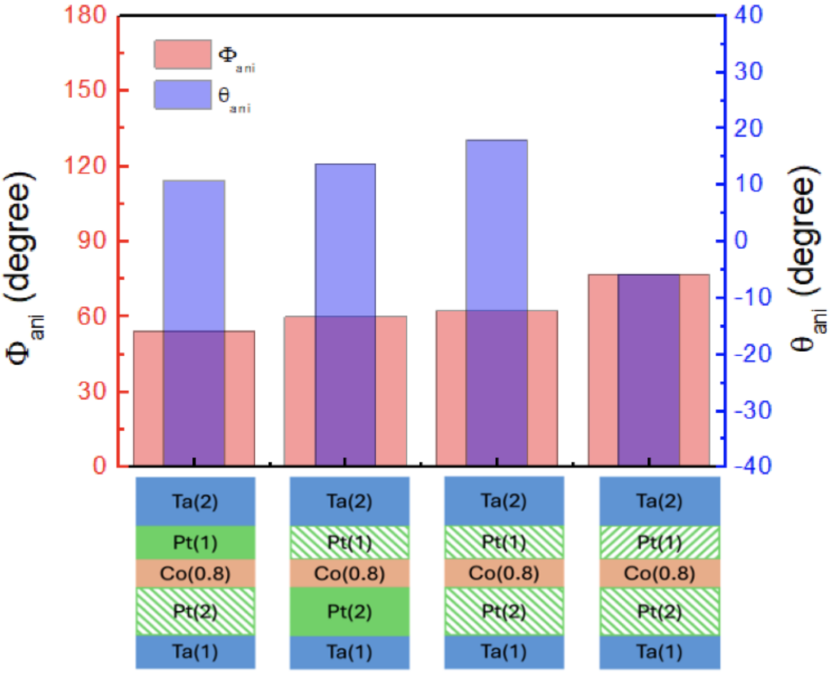

Figure 3. 12: Comparison of the azimuthal ϕ_{ani} and polar angle θ_{ani} of tilted anisotropy of upper Pt wedge, bottom Pt wedge, parallel wedge Pt and antiparallel wedge Pt sample.

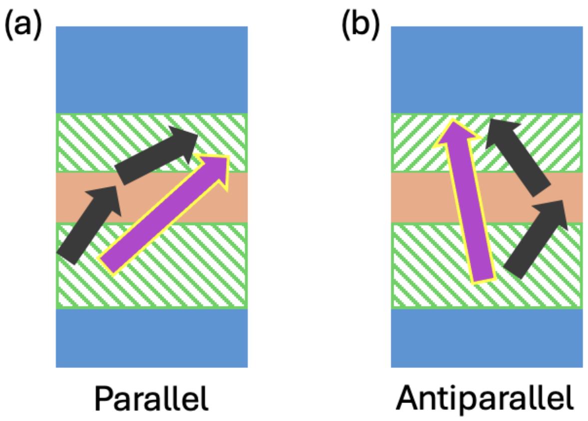

Figure 3. 13: Schematic illustration of the mechanism of tilted crystalline texture induced magnetic anisotropy of (a) parallel wedge Pt and (b) antiparallel wedge Pt.

3.5 Annealing effect on tilted PMA

For SOT magnetic tunnel junction, post deposition thermal annealing is considered a crucial process to improve the properties including the PMA, spin injection efficiency, tunnel magneto resistance ratio and the critical switching current [56][57]. Therefore, thermal annealing is carried on bottom Pt wedge sample to observe the annealing effect on field free switching and the magnetic easy axis. The annealing profile is set at 300° for 30 minutes to prevent the elimination of PMA. The AH hysteresis loop is shown in Fig. 3. 14a, note that the hysteresis loop is clear which indicate the presence of PMA, however, the coercive field H_C drops about 50% after the annealing. H^z_{eff}/I_{DC} with respect to H_x is shown in Fig. 3. 14b, the SOT behavior remains the same after thermal annealing.

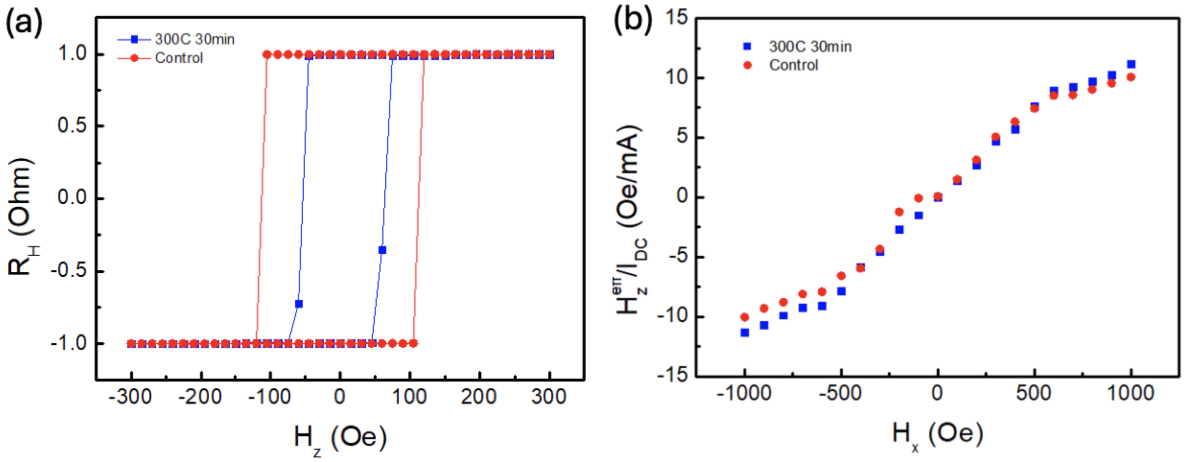

Figure 3. 14: (a) Hysteresis AH loop and (b) H^z_{eff}/I_{DC} as a function of H_x of bottom Pt wedge sample before and after thermal annealing.

Current induced SOT field free switching measurement is conducted, the representative switching loop is shown in Fig. 3. 15. The field free switching ratio of annealed sample decrease to 20% and the switching polarity is opposite to the control sample, which might be due to the remanence of the annealing instrument or the magnetization switches partially. Fixed current loop shift measurement with different in plane magnetic field is conducted to further investigate the influence on tilted magnetic anisotropy due to thermal annealing. The sinusoidal relation between $\frac{\Delta H_{SW}}{H_{IP}}$ and ϕ_H of annealed bottom Pt wedge sample is shown in Fig. 3. 16. $\frac{\Delta H_{SW}}{H_{IP}}$ is almost zero for all the ϕ_H, forming a curve with minute amplitude, indicate the magnetic easy axis is almost perpendicular to the film. The most possible reason is the atomic rearrangement and intermixing between layers sabotages the tilted texture of Pt (111), causing the magnetic anisotropy to reset to the perpendicular direction [43][58][59]. It will be a challenging task to preserve the tilted PMA after thermal annealing or even strengthen the anisotropy by specific annealing process.

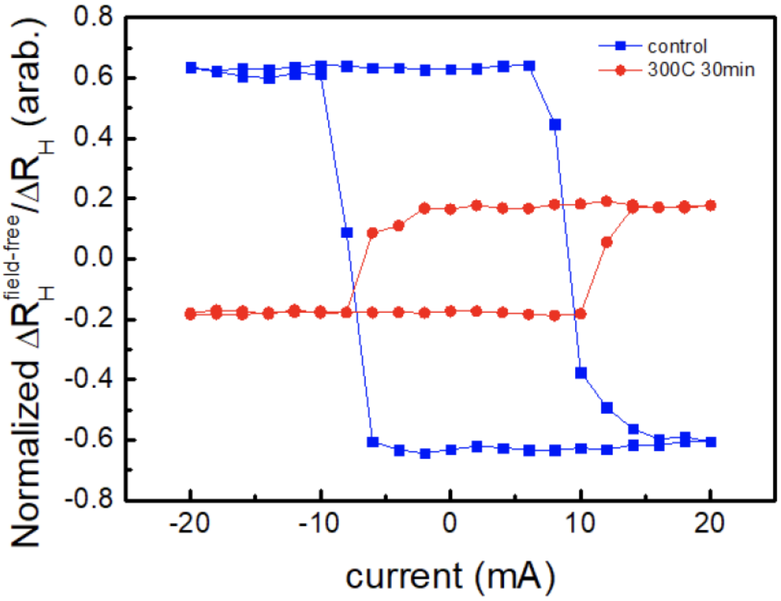

Figure 3. 15: Representative current induced field free SOT switching loops for bottom Pt wedge sample before and after annealing.

doi:10.6342/NTU202403259

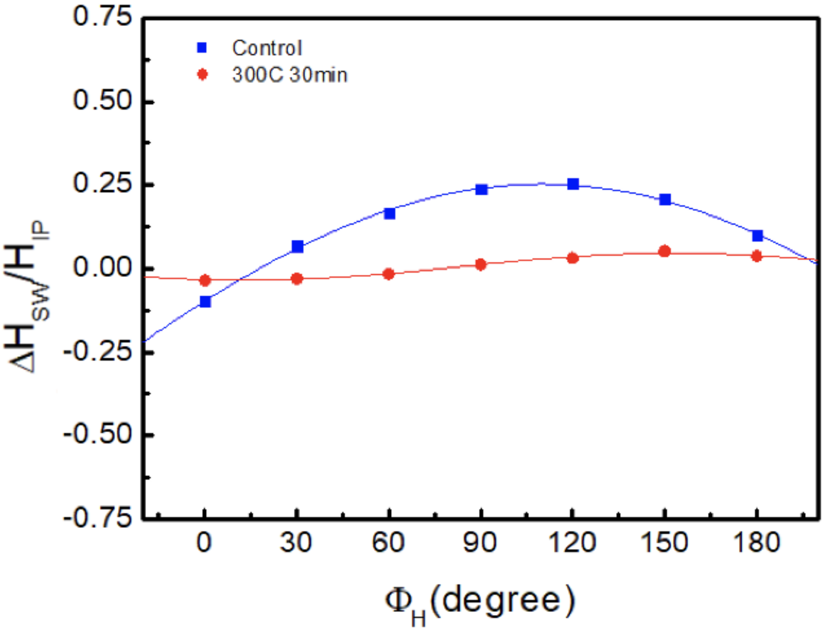

Figure 3. 16: Sinusoidal relation between $\frac{\Delta H_{SW}}{H_{IP}}$ and ϕ_H of bottom Pt wedge before and after thermal annealing, fitting by equation 3.3.

3.6 Challenges

To further utilize this structure as the free layer into practical magnetic tunnel junction (MTJ) fabrication, several ordeals must be overcome. The great spin Hall properties and good conductivity of Pt based alloys make it a competitive candidate in replacing W in CoFeB/MgO based MTJ, however, due to the lattice mismatch between Pt (FCC) and CoFeB/MgO (BCC) after thermal annealing, the PMA will be destroyed in 400°C, which is the standard temperature of back end off line (BEOL) process of CMOS fabrication. Work has reported that an insertion layer of FeTa between CoFeB and Co/Pt can improve the crystallinity of interface [60]. The crystal structure of FeTa can transform from amorphous to BCC or FCC after 400°C annealing, relying on the crystal structure of neighboring layer, which can greatly decouple the two different lattices. FeTa insertion layer also enhance the ferromagnetic coupling to strengthen the anisotropy. Another

doi:10.6342/NTU202403259

reported way is to mix 3d transition metal into Pt, which can increase the damping like torque efficiency by OHE [61]. The experiment has shown that compare to W based structure, Pt-Cr based structures manifest competitive damping like torque efficiency and better power consumption after annealed in the standard BEOL temperature.

Chapter 4 Conclusion

Summarizing the thesis, every single layer in Ta/Pt/Co/Pt/Ta is deposited in wedge condition to test the ability of field free switching and characterize the tilted magnetic anisotropy. Hysteresis loop shift measurement is utilized to observe the SOT switching properties, point out that coercive field H_C and Hall resistance difference ΔR_H remains unchanged in various wedge layers. Current induced SOT field free switching is conducted to extract the switching ratio and critical switching current. Later on, we investigate the azimuthal angle ϕ_{ani} and the polar angle θ_{ani} of the tilted magnetic easy axis, which shows a consistent result to previous report. We further conduct the same electrical measurements on wedging the upper and bottom Pt in parallel and antiparallel directions. Parallel wedge sample manifests a larger θ_{ani} which reflects on the improvement of field free switching while the antiparallel wedge sample shows a decrease in switching ratio and the reverse of switching polarity. The most persuasive reason is the enhancement and competence of two separated Pt wedge layer with the same or opposite direction. The possibility of post deposition thermal annealing in wedge structure is discussed at last. Field free switching ratio decrease significantly, and the tilted anisotropy is sabotaged after the annealing. It is reasonable to believe that the atomic rearrangement and intermixing between layer originate from annealing intermingles the tilted Pt (111) texture.

This work investigates the contribution of each layer in heterostructure (Fig. 4.1, 4.2), the discovery of combining various wedge layers also point out more possibility in

doi:10.6342/NTU202403259

tilted PMA SOT device fabrication. The preservation of tilted texture after thermal annealing will be a challenging task in the future.

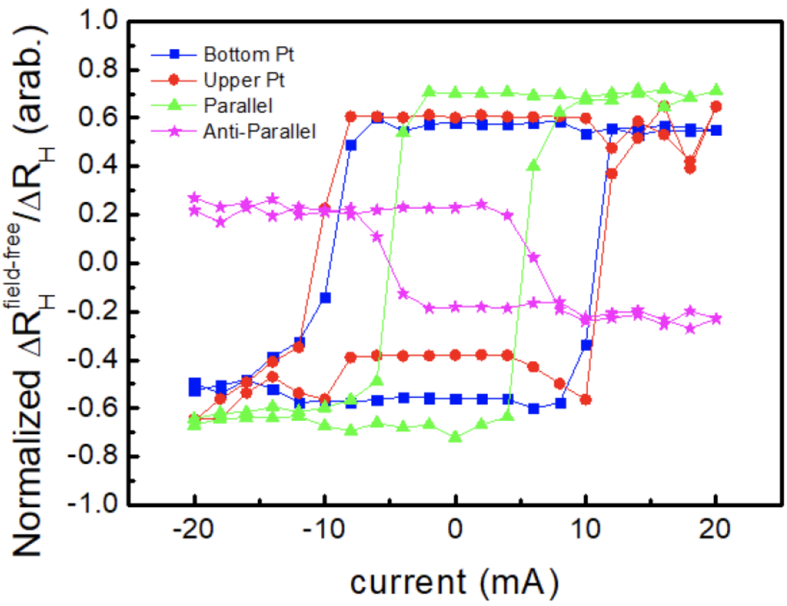

Figure 4. 1: Representative current induced field free SOT switching loops comparison for bottom Pt, upper Pt, parallel and antiparallel wedge samples.

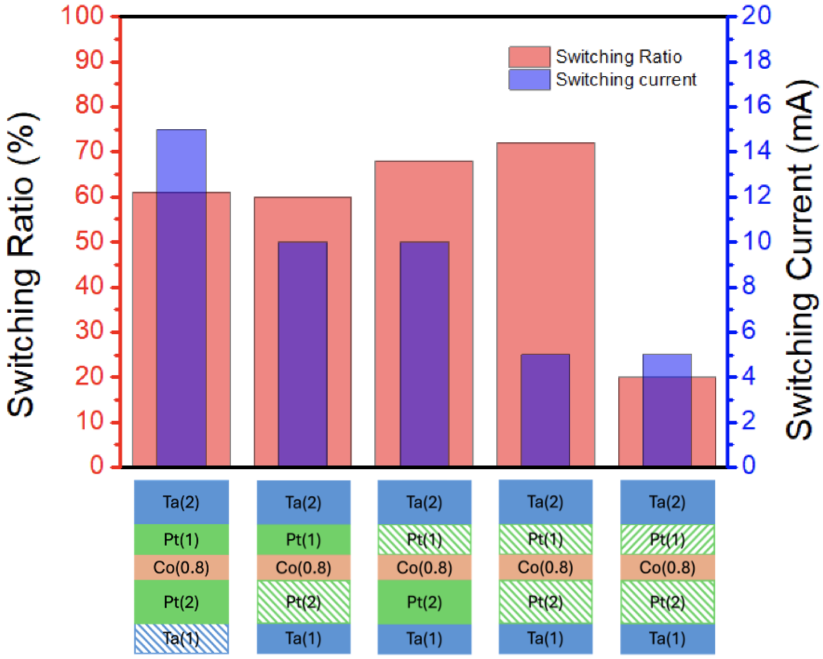

Figure 4. 2: Summary of field free switching ratio and critical switching current of seeding Ta, bottom Pt, upper Pt, parallel and antiparallel wedge samples.

References

[1] Zener, C. and Heikes, R. R. Exchange Interactions. American Physical Society, 1953.

[2] Mahduri Sharon, Goldie Oza, Arvind Gupta and Dr. Sunil Pandey. Super-paramagnetic iron oxide nanoparticles (spions) as nano-flotillas for hyperthermia. Advanced nanomaterials: synthesis, properties, and applications. Apple academic press. 2014.

[3] Cusack, N. The electrical and magnetic properties of solids: an introductory textbook. Longmans, 1958.

[4] Jungwirth, T., Marti, X., Wadley, P. et al. Antiferromagnetic spintronics. Nature Nanotech 11, 231–241, 2016.

[5] Arai, Leo & Nadeem, Muhammad & Bhadbhade, Mohan & Stride, John. A 2D cobalt based coordination polymer constructed from benzimidazole and acetate ion exhibiting spin-canted antiferromagnetism. Dalton transactions ,2010.

[6] Han, J., Cheng, R., Liu, L. et al. Coherent antiferromagnetic spintronics. Nat. Mater. 22, 684–695 ,2023.

[7] del-Río, Lucia & Nó, M. & Sota, A. & Perez-Casero, I. & Gómez Cortés, Jose & Pérez Cerrato, Mikel & Veiga, A. & Ruiz-Larrea, I. & Ausejo, Sergio & Burgos, N. & San Juan, Jose. Internal friction associated with ε martensite in shape memory steels produced by casting route and through additive manufacturing: Influence of thermal cycling on the martensitic transformation. Journal of Alloys and Compounds, 2022.

[8] Hall, E. H. On the “Rotational Coefficient” in Nickel and Cobalt. Proceedings of the Physical Society of London, 4(1), 325–342, 1880.

doi:10.6342/NTU202403259

[9] A. Yusuf, T. Adegbija and D. Gajaria, "Domain-Specific STT-MRAM-Based In-Memory Computing: A Survey," in IEEE Access, vol. 12, pp. 28036-28056, 2024.

[10] Hongming Weng, Xi Dai and Zhong Fang. From Anomalous Hall Effect to the Quantum Anomalous Hall Effect. arXiv preprint arXiv:1509.05507, 2015.

[11] Dyakonov, Michel & Perel, V. Possibility of Orienting Electron Spins with Current. Soviet Journal of Experimental and Theoretical Physics Letters. 13. 467, 1971.

[12] J.E.Hirsch. Spin Hall effect. Physical Review Letters, 83(9):1834, 1999.

[13] Y. K. Kato et al., Observation of the Spin Hall Effect in Semicon-ductors. Science306,1910-1913, 2004.

[14] Yongcheng Deng, Meiyin Yang, Yang Ji, Kaiyou Wang, Estimating spin Hall angle in heavy metal/ferromagnet heterostructures, Journal of Magnetism and Magnetic Materials, Volume 496, 2020.

[15] Chi-Feng Pai, Minh-Hai Nguyen, Carina Belvin, Luis Henrique Vilela-Leão, D. C. Ralph and R. A. Buhrman. Enhancement of perpendicular magnetic anisotropy and transmission of spin-Hall-effect-induced spin currents by a Hf spacer layer in W/Hf/CoFeB/MgO layer structures. Applied Physics Letters, 104 (8): 082407.24, 2014.

[16] Liu, Luqiao, Chi-Feng Pai, Y. Li, H. W. Tseng, D. C. Ralph, and R. A. Buhrman. "Spin-torque switching with the giant spin Hall effect of tantalum." Science, 336(6081): 555-558, 2012.

[17] Choi, YG., Jo, D., Ko, KH. et al. Observation of the orbital Hall effect in a light metal Ti. Nature 619, 52–56, 2023.

[18] Igor Lyalin, Sanaz Alikhah, Marco Berritta, Peter M. Oppeneer, and Roland K. Kawakami, Magneto-Optical Detection of the Orbital Hall Effect in Chromium, Physical Review Letters, 131, 156702, 2023.

[19] Sala, Giacomo, and Pietro Gambardella. "Giant orbital Hall effect and orbital-to-spin conversion in 3 d, 5 d, and 4 f metallic heterostructures." Physical Review Research, 4(3): 033037, 2022.

[20] Rothschild, Amit, et al. "Generation of spin currents by the orbital Hall effect in Cu and Al and their measurement by a Ferris-wheel ferromagnetic resonance technique at the wafer level." Physical Review B, 106(14): 144415, 2022.

[21] Darby, M., & Isaac, E. Magnetocrystalline anisotropy of ferro-and ferrimagnetics. IEEE Transactions on Magnetics, 10(2), 259-304, 1974.

[22] Wysin, G. M. Demagnetization fields. available on https://www. phys. ksu. edu/personal/wysin/notes/demag. Pdf, 2012.

[23] Krysztofik, A., Özoğlu, S., McMichael, R. D., & Coy, E. Effect of strain-induced anisotropy on magnetization dynamics in Y3Fe5O12 films recrystallized on a lattice-mismatched substrate. Scientific reports, 11(1), 14011, 2021.

[24] Jinnai, B., Igarashi, J., Watanabe, K., Funatsu, T., Sato, H., Fukami, S., & Ohno, H. High-performance shape-anisotropy magnetic tunnel junctions down to 2.3 nm. In 2020 IEEE International Electron Devices Meeting (IEDM) (pp. 24-6). IEEE, 2020.

[25] Tudu, B., Tian, K., & Tiwari, A. Effect of composition and thickness on the perpendicular magnetic anisotropy of (Co/Pd) multilayers. Sensors, 17(12), 2743, 2017.

[26] Bate, G., & Dunn, L. Magnetization in recorded tape. IEEE Transactions on Magnetics, 10(3), 667-669, 1974.

[27] Zhao, Z., Jamali, M., Smith, A. K., & Wang, J. P. Spin Hall switching of the magnetization in Ta/TbFeCo structures with bulk perpendicular anisotropy. Applied Physics Letters, 106(13), 2015.

doi:10.6342/NTU202403259

[28] Zhang, R. Q., Liao, L. Y., Chen, X. Z., Xu, T., Cai, L., Guo, M. H., ... & Song, C. Current-induced magnetization switching in a CoTb amorphous single layer. Physical Review B, 101(21), 214418, 2020.

[29] Yang, T., Soe, W. H., Liu, B. X., & Yamamoto, R. Perpendicular Magnetic Anisotropy and Magneto-Optical Properties of Sputtered Re-Tm (CoGd)/Pd Multilayered Films. MRS Online Proceedings Library (OPL), 458, 369, 1996.

[30] He, P., Ma, L., Shi, Z., Guo, G. Y., Zheng, J. G., Xin, Y., & Zhou, S. M. Chemical Composition Tuning of the Anomalous Hall Effect in Isoelectronic L10 FePd1-xPtx Alloy Films. arXiv preprint arXiv:1112.0834, 2011.

[31] Carcia, P. F., Meinhaldt, A. D., & Suna, A. Perpendicular magnetic anisotropy in Pd/Co thin film layered structures. Applied Physics Letters, 47(2), 178-180, 1985.

[32] Akyol, M. Origin of interfacial magnetic anisotropy in Ta/CoFeB/MgO and Pt/CoFeB/MgO multilayer thin film stacks. Journal of Superconductivity and Novel Magnetism, 32(3), 457-462, 2019.

[33] Landau, L. A. L. E., & Lifshitz, E. On the theory of the dispersion of magnetic permeability in ferromagnetic bodies. In Perspectives in Theoretical Physics (pp. 51-65). Pergamonm, 1992.

[34] Gilbert, T. L., & Kelly, J. M. Anomalous rotational damping in ferromagnetic sheets. In Conf. Magnetism and Magnetic Materials, Pittsburgh, PA (pp. 253-263), 1955.

[35] Mahmoud, Abdulqader & Ciubotaru, Florin & Vanderveken, Frederic & Chumak, Andrii & Hamdioui, Said & Adelmann, Christoph & Cotofana, Sorin. An Introduction to Spin Wave Computing. 10.36227/techrxiv.16608430.v1, 2020.

[36] Slonczewski, J. C. Current-driven excitation of magnetic multilayers. Journal of Magnetism and Magnetic Materials, 159(1-2), L1-L7, 1996.

[37] Kawahara, T., Ito, K., Takemura, R., & Ohno, H. Spin-transfer torque RAM technology: Review and prospect. Microelectronics Reliability, 52(4), 613-627, 2012.

[38] Cao, Yi & Xing, Guozhong & Lin, Huai & Zhang, Nan & Zheng, Houzhi & Wang, Kaiyou. Prospect of Spin-Orbitronic Devices and Their Applications. iScience. 23. 101614. 10.1016/j.isci.2020.101614, 2020.

[39] Song, C., Zhang, R., Liao, L., Zhou, Y., Zhou, X., Chen, R., ... & Pan, F. Spin-orbit torques: Materials, mechanisms, performances, and potential applications. Progress in Materials Science, 118, 100761, 2021.

[40] Bihlmayer, G., Rader, O., & Winkler, R. Focus on the Rashba effect. New journal of physics, 17(5), 050202, 2015.

[41] Hvazdouski, D. C., Baranava, M. S., & Stempitsky, V. R. Spin splitting in band structures of BiTeX (X= Cl, Br, I) monolayers. In IOP Conference Series: Materials Science and Engineering (Vol. 347, No. 1, p. 012017). IOP Publishing, 2018.

[42] Yu, G., Upadhyaya, P., Fan, Y., Alzate, J. G., Jiang, W., Wong, K. L., ... & Wang, K. L. Switching of perpendicular magnetization by spin–orbit torques in the absence of external magnetic fields. Nature nanotechnology, 9(7), 548-554, 2014.

[43] Hu, C. Y., Chen, W. D., Liu, Y. T., Huang, C. C., & Pai, C. F. The central role of tilted anisotropy for field-free spin–orbit torque switching of perpendicular magnetization. NPG Asia Materials, 16(1), 1, 2024.

[44] Yu, G., Chang, L. T., Akyol, M., Upadhyaya, P., He, C., Li, X., ... & Wang, K. L. Current-driven perpendicular magnetization switching in Ta/CoFeB/[TaOx or MgO/TaOx] films with lateral structural asymmetry. Applied Physics Letters, 105(10), 2014.

[45] Razavi, A., Wu, H., Shao, Q., Fang, C., Dai, B., Wong, K., ... & Wang, K. L. Deterministic spin–orbit torque switching by a light-metal insertion. Nano letters, 20(5), 3703-3709, 2020.

[46] Fukami, S., Zhang, C., DuttaGupta, S., Kurenkov, A., & Ohno, H. Magnetization switching by spin–orbit torque in an antiferromagnet–ferromagnet bilayer system. Nature materials, 15(5), 535-541, 2016.

[47] Wu, B., Jin, M., Luo, Y., Xu, X., Fan, H., Huang, H., ... & Zhou, T. Enhancement of damping-like field and field-free switching in Pt/(Co/Pt)/PtMn trilayer films prepared in the presence of an in situ magnetic field. ACS Applied Materials & Interfaces, 14(18), 21668-21676, 2022.

[48] Dzyaloshinsky, I. A thermodynamic theory of “weak” ferromagnetism of antiferromagnetics. Journal of physics and chemistry of solids, 4(4), 241-255, 1958.

[49] Wu, H., Zhang, J., Cui, B., Razavi, S. A., Che, X., Pan, Q., ... & Wang, K. L. Field-free approaches for deterministic spin–orbit torque switching of the perpendicular magnet. Materials Futures, 1(2), 022201,2022.

[50] Liu, C., Xu, J., Liu, Z., Ning, X., Jiang, S., & Miao, D. Fabrication of highly electrically conductive Ti/Ag/Ti tri-layer and Ti–Ag alloy thin films on PET fabrics by multi-target magnetron sputtering. Journal of Materials Science: Materials in Electronics, 29, 19578-19587, 2018.

[51] Pai, C. F., Mann, M., Tan, A. J., & Beach, G. S. Determination of spin torque efficiencies in heterostructures with perpendicular magnetic anisotropy. Physical Review B, 93(14), 144409, 2016.

doi:10.6342/NTU202403259

[52] Huang, C. C., Tsai, C. C., Liao, W. B., Chen, T. Y., & Pai, C. F. Deep learning for spin-orbit torque characterizations with a projected vector field magnet. Physical Review Research, 4(3), 033040, 2022.

[53] Huang, Y. H., Han, J. H., Liao, W. B., Hu, C. Y., Liu, Y. T., & Pai, C. F. Tailoring Interlayer Chiral Exchange by Azimuthal Symmetry Engineering. Nano Letters, 24(2), 649-656, 2024.

[54] Parakkat, V. M., Ganesh, K. R. & Kumar, P. S. A. Tailoring Curie temperature and magnetic anisotropy in ultrathin Pt/Co/Pt films. Aip Adv. 6, 056118 , 2016.

[55] Carcia, P. F., Li, Z. G. & Zeper, W. B. Effect of sputter-deposition processes on the microstructure and magnetic-properties of Pt/Co multilayers. J. Magn. Magn. Mater. 121, 452–460, 1993.

[56] Yu, P., Zhao, L., Gao, J., Wang, W., Luo, J., & Yang, M. Annealing effect on the magneto-electric properties of SOT-MTJs from micro to nano-sized dimensions. Japanese Journal of Applied Physics, 62(SH), SH1004, 2023.

[57] Wang, R., Jiang, X., Shelby, R. M., Macfarlane, R. M., Parkin, S. S. P., Bank, S. R., & Harris, J. S. Increase in spin injection efficiency of a CoFe/MgO (100) tunnel spin injector with thermal annealing. Applied Physics Letters, 86(5), 2005.

[58] Zhang, X., Jevasuwan, W., & Fukata, N. Interfacial intermixing of Ge/Si core–shell nanowires by thermal annealing. Nanoscale, 12(14), 7572-7576, 2020.

[59] Romano, L. T., Bringans, R. D., Knall, J., Biegelsen, D. K., Garcia, A., Northrup, J. E., & O'Keefe, M. A. Atomic rearrangement at the interface of annealed ZnSe films grown on vicinal Si (001) substrates. Physical Review B, 50(7), 4416, 1994.

[60] Yu, J., Wang, X., & Fukuzawa, H. Perpendicular magnetic tunnel junctions with a thin FeTa insertion layer for 400° C thermal stability. Applied Physics Express, 11(1), 013006, 2017.

[61] Hu, C. Y., Chiu, Y. F., Tsai, C. C., Lee, C. M., Song, M. Y., Lin, S. J., ... & Pai, C. F. Interfacial Engineering Strategies for Efficient Spin–Orbit Torque Devices with Pt Alloys. ACS Applied Electronic Materials, 5(2), 968-976, 2023.